Stress-Based and Convolutional Forecasting of Injection-Induced Seismicity: Application to The Otaniemi Geothermal Reservoir Stimulation

Taeho Kim, Jean-Philippe Avouac

California Institute of Technology

Corresponding author: Taeho Kim, tkim7@caltech.edu

Abstract

Induced seismicity observed during Enhanced Geothermal Stimulation (EGS) at Otaniemi, Finland is modelled using both statistical and physical approaches. The physical model produces simulations closest to the observations when assuming rate-and-state friction for shear failure with diffusivity matching the pressure build-up at the well-head at onset of injections. Rate-and-state friction implies a time dependent earthquake nucleation process which is found to be essential in reproducing the spatial pattern of seismicity. This implies that permeability inferred from the expansion of the seismicity triggering front (Shapiro, 1997) can be biased. We suggest a heuristic method to account for this bias that is independent of the earthquake magnitude detection threshold. Our modelling suggests that the Omori law decay during injection shut-ins results mainly from stress relaxation by pore pressure diffusion. During successive stimulations, seismicity should only be induced where the previous maximum of Coulomb stress changes is exceeded. This effect, commonly referred to as the Kaiser effect, is not clearly visible in the data from Otaniemi. The different injection locations at the various stimulation stages may have resulted in sufficiently different effective stress distributions that the effect was muted. We describe a statistical model whereby seismicity rate is estimated from convolution of the injection history with a kernel which approximates earthquake triggering by fluid diffusion. The statistical method has superior computational efficiency to the physical model and fits the observations as well as the physical model. This approach is applicable provided the Kaiser effect is not strong, as was the case in Otaniemi.

Plain Language Summary

Around 60,000 earthquakes are recorded during a span of 50 days where large volumes of water were injected underground for the stimulation of a geothermal well at Otaniemi, near Helsinki, Finland. We compare the observations with numerical simulations to analyze the physical processes that have driven these earthquakes. A model based on physics finds that it is important to use a friction law that includes friction's dependence on slip-rate and state variables to match the observations. In particular, the model allows relating the spatio-temporal evolution of seismicity with fluid pressure diffusion in the subsurface. An empirical statistical model is also developed using the recorded catalogue. The statistical model is shown to perform well in the particular case of the Otaniemi stimulations. The models provide insight into the physical processes that govern induced seismicity. The models presented in this study could help safer operations or the design of mitigation and optimization strategies that may help improve the efficiency of geothermal energy extraction.

1 Introduction

It has long been known that injection of fluids in the subsurface can induce seismicity (e.g., Healy et al., 1968; Raleigh et al., 1976; Aki et al., 1982). This issue has been put in the spotlight in recent years due to spikes of induced seismicity in regions with previously low levels of risk from earthquakes (Elsworth et al., 2016). While induced seismicity has been linked primarily to hydraulic fracturing for natural gas or 'fracking', it is also a concern in the context of geothermal energy production (Gaucher et al., 2015; Majer et al., 2007; Zang et al., 2014) and potentially carbon sequestration (Villarasa & Carrera, 2015; White & Foxall, 2016; Zoback & Gorelick, 2012). A better understanding of injection-induced seismicity is therefore of great relevance to international efforts in limiting or offsetting emissions of CO_2 (Bertani, 2012; Sander, 2011; Tester et al., 2006).

Induced seismicity is of particular relevance to geothermal energy production. Controlled hydraulic stimulation could unlock the vast geothermal resources that could be drawn from deep crustal reservoirs with no natural hydrothermal activity. Hydraulic stim-

ulation is used to enhance the heat exchange between the circulating fluids and the reservoir by creating or reactivating fractures which are hydraulically conductive. Induced seismicity is an undesirable by-product of this process, and a number of such Enhanced Geothermal Systems (EGS) has been stopped due to earthquakes felt by local residents. (Häring et al., 2008; Kwiaketk et al., 2019; Schultz et al., 2020). The development of Enhanced Geothermal Systems (EGS) would therefore benefit from better methods to forecast injection-induced seismicity.

In this study, we address this issue using a seismological dataset acquired by the Finnish company St1 Deep Heat Ltd. during an EGS operation at the Aalto University's Otaniemi campus near Helsinki (Hillers et al., 2020; Kwiatek et al, 2019; Leonhardt et al., 2021). A large catalogue produced with Machine Learning techniques (Ross et al., 2018a, 2018b) revealed that the time evolution of seismicity can be predicted well based on a simple convolution model (Avouac et al., 2020). An enhanced catalogue was also recently produced by Leonhardt et al. (2021). Building on this previous work, we present and assess physical and statistical models to forecast the spatio-temporal evolution of seismicity induced by the Otaniemi EGS stimulation.

2 Injection-Induced Seismicity: Mechanisms And Forecasting Methods

Induced seismicity can result from either a stress or strength change on a fracture or fault. The effect of injection is generally assessed by considering pore pressure diffusion in the medium and the consequent decrease in the effective normal stress as according to Terzaghi's principle (Skempton, 1984). This first-order description of the stress state has been effective in explaining various aspects of induced seismicity, including the $\sqrt{t}$ evolution of the seismicity front (Shapiro et al., 1997, 2006) and general spatiotemporal patterns of induced seismicity (Elmar & Shapiro, 2002; Shapiro et al., 1999, 2002) as early as the pioneering study at the Rangely oil field (Raleigh et al., 1976). An additional step in the description of stress changes due to a fluid injection is the theory of poroelasticity which describes the coupling between fluid flow and deformation of the solid skeleton. Poroelasticity has been shown to play a role in triggering earthquakes in addition to pore pressure evolution (Segall, 1989; Segall et al. 1994; Segall & Lu, 2015), particularly outside the characteristic pore pressure diffusion length (Goebel & Brodsky, 2018; Zbinden et al., 2020). Although the magnitude of stress changes from poroelasticity is estimated to account for typically only about a tenth of that from pore pressure diffusion (Zhai & Shirazei, 2018), its consideration is often required for complete explanations of the observed seismicity in space and time.

A fluid injection can result in 'hydrofractures' (Mode-I opening fractures) or shear fractures (Mode-II or Mode-III). Induced earthquakes generally result from shear failure. While linear elastic fracture mechanics is commonly employed in modeling the growth of cracks in Mode-I and the consequent stress changes, modeling shear failure requires an appropriate friction law. One kind of models is based on the Mohr-Coulomb failure criterion in which slip occurs once the ratio of the shear stress to the normal stress on a fault reaches a pre-defined threshold, the static friction coefficient, and drops to the dynamic friction coefficient either at the immediate onset of slip or gradually with fault slip. However, there is ample evidence from laboratory studies and natural observations that the initiation of slip involves in fact a gradual decrease of friction associated with asesimic slip, often referred to as the nucleation process. Such an evolution of friction is commonly described using the rate-and-state friction law derived from frictional sliding experiments in the laboratory (Ampuero & Rubin, 2008; Dieterich, 1994; Dieterich & Linker, 1992; Marone, 1998; Ruina, 1983).

The non-instantaneous nucleation process implied by rate-and-state friction can explain a number of phenomenological observations such as the Omori decay of seismic-

ity rate during aftershocks (Dieterich, 1994) or the low sensitivity of seismicity to solid-earth tides (e.g., Beeler and Lockner, 2003). The rate-and-state formalism has also shown success in explaining the relationship between stress and seismicity rate due to diking (e.g., Toda et al., 2002) and aseismic slip (e.g., Segall et al., 2006). In the context of induced seismicity, rate-and-state friction has been applied to explain certain non-linear features such as the time lag between induced seismicity and stress perturbations (e.g., Dempsey and Riffaut 2019; Candela et al. 2019; Norbeck & Rubinstein 2018; Richter et al. 2020). It is important to note that, in principle, the activation of a fault by a pore pressure increase doesn't necessarily imply seismic slip (e.g., Guglielmi et al., 2015). In fact, there is observational evidence that injection-induced fault slip is mostly conditionally stable (Bourouis & Bernard, 2007; Calò et al., 2011; Guglielmi et al., 2015; Goodfellow et al., 2015; Scotti & Cornet, 1994), as is expected from the nucleation model based on rate-and-state friction and that seismicity is in fact occurring outside the zones of high pore pressure (Cappa et al., 2019; De Barros et al., 2018; Wei et al., 2015).

More specifically with regards to hydraulic stimulation of geothermal wells, important questions arise regarding the differences between the Mohr-Coulomb and rate-and-state friction-based models considering the rapid stressing rate that is common in such operations. Mohr-Coulomb models coupled with linear slip weakening can result in realistic simulations of seismic ruptures while accounting for the nucleation process (Olsen et al, 1997). This is not the case for single-degree-of-freedom spring-slider systems often employed for modelling induced seismicity. The commonly used model of Dieterich (1994) based on rate-and-state friction can converge to models based on the Mohr-Coulomb criterion at the rapid equilibrium limit. It is also possible that rate-and-state effects on nucleation may be significant at the relatively short timescale of intense injection cycles during stimulation.

A hysteresis effect, often referred to as the Kaiser effect, is also commonly observed in induced seismicity. The Kaiser effect refers to the observation when a material submitted to a series of loading cycles of increasing amplitude fails gradually, further failure generally occurs at a stress level exceeding the maximum stress reached in previous cycles. This effect explains the observation that acoustic emissions during rock failure stop if the stress decreases and do not resume until the medium is loaded to its previous maximum (Lavrov, 2003). How a nucleation source "remembers" its loading history has proven to be essential in reproducing various observations in induced seismicity, such as time delays of the seismicity rate in response to perturbations of the injection rate and regions of seismic quiescence behind triggering fronts (Baisch et al., 2006, 2010; Dempsey & Riffault, 2019).

Numerous physical models have been developed to incorporate stress changes, pore-pressure changes and failure mechanisms in a single framework (Gaucher et al., 2015; Grigoli et al., 2017). A notable example of physical models that accounts for rate-and-state friction in particular, is presented by Segall & Lu (2015), where changes in stresses by fluid injections into an infinite poro-elastic medium were used as input to the model of Dieterich (1994), relating seismicity and stress rates among a population of nucleation sources. Although the framework was originally used to investigate poroelastic effects during shut-in and to address the common observation that maximum magnitude events often occur after injections cease (Grigoli et al., 2018; Häring et al., 2008), it can be used more generally to study induced seismicity in response to various injection scenarios (e.g., Zhai & Shirzaei, 2018). Finite-fault and fracture network models accounting for rate-and-state friction have also been developed (Almakari et al., 2019; Dublanchet, 2018; Larochelle et al., 2021; McClure & Horne, 2011) to examine rupture properties and the effect of heterogeneous fault properties on the seismicity rate. Numerous factors make it difficult, however, to resort to such models in practice, such as the high computational cost of solvers and poor resolution of pre-existing heterogeneities in the sub-surface - in particular, the distribution of stress and strength - with a level of detail that cannot be constrained with

observation. Some representations of heterogeneities are essential in reproducing well-established statistical properties of earthquakes (Zoller et al., 2005; Dempsey et al., 2016) such as the Gutenberg-Richter law which describes the magnitude-frequency distribution of earthquakes (Gutenberg & Richter, 1956).

Due to the complexity of stress-based models along with the difficulty to calibrate the model parameters, a number of studies have alternatively explored data-driven statistical modeling. Such models often hinge on the Gutenberg-Richter law (Gutenberg & Richter, 1956) and the assumption that earthquakes follow a Poisson process. Additionally, they often model earthquake triggering as a cascading process based on the Omori law (Utsu, 2002) which fits commonly observed patterns of the decay of seismicity rate during aftershock sequences. A popular example is the epidemic type aftershock model (ETAS) (e.g., Ogata, 1988), which represents the total seismicity as a linear superposition of homogeneous Poisson processes, to represent mainshock and aftershock sequences (e.g., Bachmann et al., 2011; Lei et al., 2008; Mena et al., 2013). Such models have the advantage of resulting in very realistic synthetic catalogs since they incorporate statistical properties directly derived from observations. However, statistical approaches are in principle less transportable from one reservoir to another as they lack explicit connections to the mechanical and hydro-geological properties of the medium. The development of hybrid models that account for the complex network of physical mechanisms while being generalizable and applicable to various injection sites and scenarios is therefore an active area of research (Gaucher et al., 2015).

3 Data Presentation And Analysis

The seismic catalogue analyzed in this study comes from a geothermal well stimulation project operated by St1 Deep Heat Ltd. near the campus of Aalto University in Otaniemi, Finland and is compiled by Leonhardt et al. (2021). The injection well (OTN-3 in Figure 1) was drilled to a depth of 6.1 km into Precambrian crystalline (gneiss and granite) rocks. Approximately 18,000m^3 of water was injected over the course of 49 days from June 4th to July 22nd in 2018. The injection history was divided into five successive stages moving upward from the bottom of the well (Figure 1). Pumping parameters of the injection such as the injection rate and well-head pressure were tuned as part of a Traffic Light System (TLS), the details of which are presented in Ader et al. (2020) and Kwiatek et al. (2019). The stimulation consisted of numerous cycles of injections and pauses of varying duration. The injection history also included periods of bleed-off's where injection was stopped and backflow out of the well was allowed.

The stimulations were monitored with surface and borehole seismometers providing excellent detection and location of the induced earthquakes (Hillers et al., 2020; Kwiatek et al., 2019). Namely, the monitoring network consisted of a seismometer array at 2.20-2.65km depth in a separate well (OTN-2), located around 400 m from OTN-3, in addition to a 12-station network installed in 0.3-1.15 km deep wells (Figure 1). The catalogue consists of 61,150 events in total (Figure 2) and 1986 relocated events with spatial uncertainty of ±52m (Figure 3). The magnitude of completeness is estimated to be M_c = -1.1.

A few salient features of the observed seismicity guide our modeling. First, the seismicity rate has a positive correlation to the injection rate in time, accompanied by finite periods over which it increases and decreases in response to injections and shut-ins, respectively. We indeed note that the seismicity rate reaches a similar magnitude for injections far apart in time but equal in the flow rate. Second, the decay pattern in the seismicity rate, R, during injection pauses is well-matched by the Omori law

$$R(t) = \frac{R_0}{1 + t/t_r}, \tag{1}$$

where t is time, t_r is the time it takes for the seismicity rate to halve, and R_0 is the seismicity rate at the onset of decay. A fit to one of the injection pause periods is shown in Figure 4. Note that the more general 'modified Omori law' (Utsu, 2002) allows a $1/t^p$ decay of seismicity rate; here the p-value is close to 1. The close match to the Omori law is consistent with observations of the decay rate in induced seismicity following shut-ins reported in a number of previous studies (Almakari et al., 2019; Bachmann et al. 2011, 2012; Langenbruch & Shapiro, 2010). Lastly, the relocated catalogue (Figure 3) shows a rather diffuse distribution of seismicity, suggesting that the injection stimulated fractures were distributed within a relatively large volume ($\sim 1\text{km}^3$) around the open sections of the well by diffusion of pore pressure.

The exact origin of Omori law decay remains poorly understood; it could be due to the finite nucleation process governed by rate-and-state friction (Dieterich, 1994) or by instantaneous nucleation and postseismic creep that predict a p-value of approximately 1 (Perfettini and Avouac, 2004). This process was suggested to have occurred during a 10 MPa stimulation of a geothermal well at $\sim$ 3km depth at Soultz-sous-Forêt (Bourouis and Bernard, 2007). Similarly, stress relaxation by pore pressure diffusion (Nur & Booker, 1972) predicts a seismicity decay also closely resembling the Omori law with a p-value typically between 1 and 2 (Langenbruch & Shapiro, 2010; Miller, 2020). Studying the properties of the Omori-like decay provides a valuable opportunity to re-examine its mechanical origins and the physical mechanisms that drive induced seismicity.

4 Linear Transfer Function and Convolution Model

The direct relationship between the injection and observed seismicity rate suggests that it may be represented by a linear transfer function of the injection history (Avouac et al., 2020). To quantify this relationship, we use the algorithm of Marsan & Lengline (2008) which was originally designed to determine the kernels characterizing how earthquakes trigger other earthquakes. The algorithm estimates weights as a function of distance and time which, after normalization, represent the probability that any earthquake was triggered by any previous earthquake. We adapted the algorithm here to determine the weight relating earthquakes to injections as the source of trigger. As justified later on, secondary triggering is ignored (i.e., aftershocks of triggered events are ignored). We assume that the observed seismicity rate density, $\lambda(x,t)$, or the number of earthquakes in unit time can be modelled by a linear superposition of the influence from all previous injections such that

$$\lambda(t) = \lambda_0 + \sum_{t_i<t} \lambda_i(t), \tag{2}$$

where λ_0 is the uniform background rate density, and $\lambda_i(t)$ represents the rate density at time t incurred by injection i. A non-linear behaviour may in reality arise from the possible coupling between fluid pressure and permeability, and from the seismicity model. Rate-and-state friction and the Kaiser effect are indeed sources of non-linearity, as we discuss in greater detail below.

The kernel $\lambda(\Delta t)$ (referred to as the bare rates) that defines $\lambda_i(t)$ is found through an iterative process: First, we begin with an initial guess for $\lambda(\Delta t)$ and compute the triggering weights between injection i and event j, $w_{i,j} = \alpha_j \lambda(t_j - t_i)$ and the background weight $w_{0,j} = \alpha_j \lambda_0$ where α_j is a normalization coefficient to satisfy that $\sum_{i=0}^{j-1} w_{i.j} = 1$. Here, $w_{i,j} = 0$ if $t_i > t_j$ (earthquakes cannot be triggered by future injections). Secondly, $\lambda(\Delta t)$ is updated as follows

$$\lambda(\Delta t) = \frac{1}{N \cdot \delta t} \sum_{i,j \in A} w_{i,j}, \tag{3}$$

where A is the set of pairs such that $|t_j - t_i| \leq \delta t$, and N is the number of total earthquakes. Thus, δt becomes the discretization parameter of the algorithm. The two main assumptions of the model are linearity of the rate density that allows superposition of λ_i and the existence of a mean-field response to injections that is independent of event magnitude or injection volume. Demonstration of the algorithm on a simple synthetic catalogue and its sensitivity to discretization parameters are illustrated in the Supplementary Text S1.

Injections are divided into individual cycles by binning them into regular 10-minute intervals. The result reveals a time decay proportional to $1/t$ (Figure 5). This is consistent with the observed Omori law decay following shut-ins and also with the period of build-up in seismicity at the beginning of injections. It is also possible to use this approach to estimate spatial kernels. The results are not presented here as we found the size of the dataset and the quality of the locations to be insufficient to get well constrained kernels.

The observation that the response to step-like decrease of injection rate leads to a $1/t$ Omori law decay can be used to estimate a Green's function, $g(t)$ (Avouac et al., 2020). Since the derivative of a step function is a Dirac delta function, $g(t)$ can be found by simply differentiating the Omori law in time

$$g(t) = -\frac{d}{dt}\left(\frac{R_0}{1 + t/t_r}\right) = \frac{R_0/t_r}{(1 + t/t_r)^2} \tag{4}$$

The predicted seismicity rate can then obtained from a simple convolution

$$R(t) = u(t) * g(t) = \int_{-\infty}^{\infty} u(\tau) g(t - \tau)\, d\tau, \tag{5}$$

where R and u are the seismicity and injection rate, respectively. Bleed-off's are implemented as negative injection rates (likewise to all forthcoming models in this study). To construct the kernel for the specific case of Otaniemi, t_r is chosen by fitting the Omori law to the last of the injection pauses of durations significantly longer than the average injection cycle (about 20 hours). Then, R_0 is determined so as to yield a total number of events equal to the number of earthquakes in the catalog. t_r and R_0 are found to be 24.1 hours and 208.9 events per hour, respectively. Although Avouac et al. (2020) reported that the data suggests a systematic increase of t_r during the stimulation likely due to the increasing volume of the domain of increased pore pressure, we use a constant value of t_r as the resulting difference to the fit is minor.

The model result is displayed with the observed catalogue in Figure 6a. It follows remarkably well the observed seismicity rate variations; bulk of the observed seismicity is included within the 95% confidence interval, calculated by assuming events are governed by an non-homogeneous Poisson process following the modelled seismicity rate. The model also closely matches the decay rate during injection pauses and the build-up rate at the onset of injection cycles.

To quantify the goodness of fit, we use both the Kolmogorov-Smirnov test (Massey, 1951) and the Poisson log-likelihood (Dempsey & Suckale, 2017). The Kolmogorov-Smirnov test returns the KS-statistic, which is the maximum difference between the cumulative distribution functions given by the prediction and the observation. The Poisson log-likelihood is the appropriate metric if earthquakes are assumed to result from a Poisson process, even if inhomogeneous in the case the rate varies in time and space. So the metric is valid as long as secondary aftershocks can be ignored. This assumption is tested by analyzing the distribution of interevent distances in space and time using the method of Zaliapin and Ben-Zion (2013). The result is shown in Supplementary Figure S4, which displays a uni-modal distribution instead of the bi-modal distribution that would be expected

in case of clustering due to aftershock sequences. This is consistent with the analysis by Kwiatek et al. (2019) which shows that aftershocks account for no more than 10% of the events in their seismicity catalogue and the observation that aftershock sequences are rarely observed in seismicity induced by hydraulic stimulations (e.g., Baisch & Harjes, 2003). One advantage of the Poisson log-likelihood and the Kolmogorov-Smirnov test is also that the metrics don't require binning of the point process (Dempsey & Suckale, 2017). Binning is used in the figures only for convenience to represent the data. The log-likelihood function is given by

$$\mathrm{LLK}(\theta) = \sum_{j=1}^{n} \log R(\theta; t_j) - \int_0^{t_n} R(\theta; t')dt', \tag{6}$$

where θ is the set of model parameters and t_j is the occurrence time of event $j = \{1, 2, ..., n\}$. We report the KS-statistic here, preferred to the log-likelihood which is sensitive to the choice of units for R, but we see good qualitative agreement between the two measures as summarized in Table 2. The KS-statistic for the convolution model returns 0.036. The quality of the fit is impressive considering the simplicity of the model – which involves only two parameters. It also contradicts the premise that various non-linear mechanisms driving induced seismicity, such as the non-linearity of rate-and-state friction, the Kaiser effect, and changes in permeability due to high pore pressure and the development of hydraulic fractures, should result in a nonlinear response overall. It may be that non-linear effects in Otaniemi are in fact small despite the relatively large stress variations induced by hydraulic stimulation, the possibility of which we explore with our physical models later on and in the supplementary materials.

5 Physical Modeling

We now present a physical model based on stress evolution from pore pressure diffusion and poroelasticity along with shear failure criterion following rate-and-state friction. The medium is treated to be infinite, homogeneous and isotropic. Neglecting the effect of the free surface is justified by the relatively large depth of the injections compared to the dimensions of the seismicity cloud (Figure 3). The induced stresses can then be calculated using the analytical solutions for a point source from Rudnicki (1986)

$$p(r,t) = \frac{q}{4\pi\rho_0 r}\frac{\eta}{k_{true}}\,\mathrm{erfc}\Big(\frac{1}{2}\xi\Big), \tag{7}$$

$$\sigma_{ij}(r,t) = -\frac{q(\lambda_u-\lambda)\mu}{4\pi\rho_0 c_{true} r\alpha(\lambda_u+2\mu)} \left\{\delta_{ij}\left[\mathrm{erfc}\Big(\tfrac{1}{2}\xi\Big) - 2\xi^{-2}f(\xi)\right] + \tfrac{x_i x_j}{r^2}\left[\mathrm{erfc}\Big(\tfrac{1}{2}\xi\Big) + 6\xi^{-2}f(\xi)\right]\right\}, \tag{8}$$

$$f(\xi) \quad = \mathrm{erf}(\tfrac{1}{2}\xi) - \tfrac{\xi}{\sqrt{\pi}}\exp(-\tfrac{1}{4}\xi^2),$$

$$\xi = \frac{r}{\sqrt{c_{true}t}},$$

$$c_{true} = \frac{k_{true}}{\eta}\frac{(\lambda_u-\lambda)(\lambda+2\mu)}{\alpha^2(\lambda_u+2\mu)},$$

where p and σ_{ij} are the pore pressure and stress tensor, and r and t the distance from injection source and time, respectively; $\lambda_u = 2\mu\nu_u/(1–2\nu_u)$ is the undrained Lamé parameter and the drained Lamé parameter without the subscript u; c is the hydraulic diffusivity which depends on permeability, k and viscosity, η. Here we add the subscript "true" to k and c to distinguish between the true and apparent values of the diffusivity, the notions of which are explored in greater detail by our following analysis. We assume the point source is a good approximation of the injections in Otaniemi given the length of the stimulated wells relative to the size of the total stimulated volume. The model is nearly identical to that introduced by Segall & Lu (2015). Poroelastic properties which lack constraints from the field, along with a fixed fault-orientation are chosen as those in Segall & Lu (2015) to represent a general case. Ambient normal stress of 155 MPa is approximated using the average depth of the injection. All fixed parameters and their dimensions are listed in Table 1.

Stress changes become the input to the ODE formulation of Dieterich (1994), to solve for seismicity rate in space and time. The alternative integral formulation of Heimisson & Segall (2018) is used here as it is more tractable numerically for injection scenarios such as in Otaniemi that consist of abrupt onsets and shut-ins of injections

$$\frac{R}{r_b} = \frac{K(t)}{1 + \frac{1}{t_a}\int_0^t K(t')\, dt'}, \tag{9}$$

$$K(t) = \exp\left(\frac{\tau(t)}{a\overline{\sigma}(t)} - \frac{\tau_0}{\overline{\sigma}_0}\right),$$

$$t_a = \frac{a\overline{\sigma}_0}{\dot{\tau}_r},$$

$$\overline{\sigma} = \sigma - p,$$

where r_b is the background seismicity rate, $\dot{\tau}_r$ the background stressing rate, a the rate-and-state friction parameter, σ the normal stress, $\overline{\sigma}_0$ and τ_0 the initial effective normal and shear stress, and $\overline{\sigma}$ and τ the applied effective normal and shear stress, respectively. Synthetic catalogues are produced by sampling events from a non-homogeneous Poisson process using the acceptance-rejection method.

The Kaiser effect is inherent in the formulation of Dieterich (1994) and Heimisson & Segall (2018). This results from the fact that the nucleation process is delayed if the stress decreases and resumes once the stress gets back to its previous peak level. The Kaiser effect is clearly demonstrated if we use the model to compute the response of the seismicity rate to a sinusoidal stressing history (Supplementary Figure S5). The different injection locations must stimulate new volumes of rock and lead to new hydraulic pathways. So we might expect the Kaiser effect to be significant within a single stage but to be less relevant from one stage to the other. The impact of the Kaiser effect may be more appropriately represented by resetting the stressing history at the onset of each stage. To this effect, we start a new simulation with the same initial conditions and compound the results for the final catalogue. This model is hereafter referred to as the rate-and-state model. Note that the validity of resetting the stress history could be questioned given that the seismicity clouds during the different stages largely overlap (Figure 3) suggesting overlapping stimulated volumes.

We use the measured flow rates and pressure to estimate hydraulic diffusivity. An estimate of the diffusivity that fits the rate of pressure decay during injection pauses is

made by the Horner analysis. Since the analytical solutions of the present model are derived for spherical flow in a 3-D medium, the conventional Horner analysis originally derived for 2-D flow into a vertically confined aquifer (Horne, 1995; Zimmermann, 2018) is adapted to be consistent with Equations (7) and (8). Details on the adaptation and fitting process are presented in the Supplementary Text S2. The analysis gives a diffusivity of $c_{horner} = 0.018$ m^2/s, and a global fit to the entire pressure history using a Gaussian likelihood function gives an effective well radius and ambient pore pressure of 44m and 43.5MPa, respectively. The model fits the measured pressure history well during the entire stimulation, especially during the injection pauses (Figure 7a). A fit to the pressure history with diffusivity as a free parameter, however, gives a higher value of $c_{bu} = 0.044$ m^2/s (subscript '*bu*' standing for "build-up") that better matches the rate of pressure build-up at the onset of injection cycles (Figure 7b) with an effective radius and ambient pore pressure of 31m and 54.9MPa, respectively. c_{bu} also over predicts the rate of pressure decay during injection pauses. While constraints on the effective radius - a measure of the damage zone surrounding the well that causes pressure drops - are difficult to quantify, ambient pore pressure in either cases are close to its bounds considering the temperature-dependence of fluid density at injection depth. When comparing the theoretical triggering front derived by Shapiro (1997), i.e. $r = \sqrt{4\pi c_{tf} t}$ where c_{tf} is the diffusivity chosen to draw the triggering front, c_{horner} appears to fit the spatial extent of near-field events better (Figure 3). We therefore use $c_{horner} = c_{true}$ as a starting point for the models and refer to its theoretical triggering front as the 'reference triggering front'. We revise this assumption later and note that the diffusivity derived from the Horner analysis fits the pressure drop at shut-ins, as should be the case by design, but doesn't match the pressure build-up when injections start again (Figure 7a).

The posterior distribution on the set of parameters associated to the seismicity model $a, \dot{\tau}_r$, and r_b is found using the affine invariant Markov chain Monte Carlo (MCMC) Ensemble sampler of Goodman & Weare (2010) maximizing the log-likelihood given by Equation (6). In order to simplify the sampling process, the sampler computes the posterior of a and $\dot{\tau}_r$ given that r_b - which is a simple multiplicative factor to the normalized seismicity rate - is adjusted for each pair of a and $\dot{\tau}_r$ to match the total number of observed events (61,150 events). The sampler conducts 2000 $\sim$ 5000 iterations of 32 walkers with the chain length made to be longer 50 times the auto-correlation length in order to ensure full exploration of the posterior distribution. The prior is assumed to be uniform for both variables between the range of $10^{-5} \sim 10^{-2}$ and 0.1 kPa/yr. $\sim$ 5 kPa/yr. for a and $\dot{\tau}_r$, respectively, although the shape of the prior is seen to have little effect on the posterior given the large sample size.

$a, \dot{\tau}_r$, and r_b of maximum likelihood is found to be 0.0002, 3.05 kPa/yr. and 12.1 events/days, respectively, and the resulting model is shown in Figure 6b. The model follows the observations quite well in time, with a KS-statistic of 0.029, slightly lower than the value of 0.036 obtained with the convolution model. The model succeeds in reproducing the main temporal features of the observed catalogue: 1. direct correlation between the injection and seismicity rate and 2. Omori-law decay during shut-ins. In space, the fit is much less compelling (Figure 8b). The triggering front lags significantly behind the reference triggering front with a much smaller mean of the distribution. Yet in both time and space, resetting of the stress history at each injection stage turns out to be essential in reproducing important features of the observation. The best fit using the model without resetting of the stress history ($a = 0.0001$, $\dot{\tau}_r = 4.89$ kPa/year, and $r_b = 25.9$ events/day) as shown in Figure 6c has relatively minimal seismicity rate during the second half of the injection history due to the Kaiser effect. In space, it is completely devoid of any seismicity close to the injection well during this period (Figure 8c). Far-field seismicity much beyond the reference triggering front is largely attributed to background stressing as poroelastic stress perturbations are small relative to pore pressure changes.

6 Adjusting Model Diffusivity to Spatio-temporal Distribution of Seismicity

Given that the rate-and-state model fails to match the observations in space assuming the diffusivity inferred from Horner analysis, we now examine the possible underestimation of the diffusivity by the Horner analysis. Following the seminal study of Shapiro (1997), it has become common practice to infer the diffusivity from fitting $r = \sqrt{4\pi c_{tf} t}$ to the propagation of the seismicity front, or the triggering front - defined by the outline of the outermost events of the seismicity cloud extending from the well. However, we note that c_{tf} of the rate-and-state model shows a significant mismatch by a factor of $\sim$3 from $c_{true} = c_{horner}$ prescribed in the model (Figure 8b). This discrepancy is due to the role of delayed nucleation represented by $a\sigma$. As shown by Wenzel (2017), the parameter $a\sigma$ of the rate-and-state model acts as a threshold triggering stress that restricts the extent of the triggering front. The sensitivity of the triggering front to $a\sigma$ is clearly visible in Figure 9 which compares two synthetic catalogues that only differ in the prescribed values of a. In the scope of the rate-and-state model or stress thresholds as commonly used in Mohr-Coulomb models, inference of the diffusivity from the apparent migration of seismicity requires considerations of both c and a. Additionally, the method of inferring the diffusivity from the triggering front may depend on the earthquake detection thresholds. A higher detection threshold may give a more poorly resolved catalogue in space that could lead to a different estimation of the triggering front. Furthermore, the position of the triggering front can be obscured even more by background seismicity and far-field events triggered by poroelastic effects. Fitting the seismicity front represented by the envelope of the seismicity cloud, places a lot of weight on potentially biased and not particularly well-defined features.

In consideration of such complications, one would wish for a definition of the seismicity front that is independent of the number of events in the catalogue and robust to factors of discrepancy between observations and model predictions. We therefore propose an approach to infer c_{true} from the spatial distribution of the seismicity as opposed to the triggering front. A simple way is to fit the distribution as a function of distance and time from the point of injection with a known analytical expression. We recall that the half-norm distribution is the solution to the diffusion equation in response to a Dirac point source in a 3-D medium where the standard deviation of the distribution, $\Lambda(t)$, is a function of time such that

$$f_Y(y; \Lambda(t)) = \frac{\sqrt{2}}{\Lambda(t)\sqrt{\pi}} \exp\left(- \frac{y^2}{2\Lambda(t)^2} \right) \quad , \quad y \geq 0 \tag{10}$$

This inspires our approach to fit Equation (10) to the rate-and-state model in response to a constant injection scenario. The half-norm distribution indeed turns out to provide a relatively good fit (Figure 10); it matches well the bulk of the distribution but tends to slightly overestimate seismicity rate at larger distances. Indeed, we do not make the claim that the half-norm distribution is the best possible fit and acknowledge there may be other distributions that could better match the rate-and-state model although they are not explored further here. Furthermore, plotting the evolution of Λ versus time reveals that it follows closely $\sqrt{c_{true} t}$. We make the assumption that the remaining discrepancy can be modelled as a multiplicative factor such that

$$\Lambda(t) = \sqrt{c_{hg} t} = \sqrt{\gamma(\{l\}) c_{true} t}, \tag{11}$$

where $\{l\}$ is a set of non-dimensional parameters. Thus, c_{hg} is a measure of the radial spreading of the seismicity relative to the point of injection ('hg' standing for half-Gaussian distribution). In order to apply this method to Otaniemi, we attempt to estimate c_{hg} from the relocated catalogue. One disadvantage of the method is that it requires a set

of relocated events large enough to constrain the evolution of c_{hg} with confidence. As detailed in the supplementary text S3, we can indirectly estimate from the cumulative relocated catalogue giving $c_{hg} = 0.011$ m^2/s (Supplementary Figure S6).

We find the relationship $\gamma_h(l)$ empirically by observing the systematic dependence of γ_h on l as reproduced by the rate-and-state model. We assume l depends not only on pore fluid transport properties but also rate-and-state properties such as a. We find to be relevant the ratio $l = a\sigma/p_q$, where $p_q = \frac{q\eta}{4\pi\rho_0 kL}$ is the characteristic pore pressure for given injection rate q, and L is the size of the computational domain. Higher values of $a\sigma$ would produce a stronger threshold effect and suppress seismicity migration, the extent of which would depend on its strength relative to the induced pressure, p_q. A series of single boxcar injections are simulated for a range of c and a. We find a rational function of $a\sigma/p_q$ that fits γ_h as shown in Figure 11. Although the reason for the exact functional form of the relationship is not obvious, the quality of the fit is compelling. The observed trend is also consistent with the known role of $a\sigma$: higher values of a suppresses seismicity at further distances, decreasing c_{hg} and consequentially γ_h. The functional fit allows new uncertainty estimates of the diffusivity in Otaniemi. Figure 11 shows the difference between the predicted and true values of diffusivity for a range of c_{true} and a, given the estimated value of $c_{hg} = 0.011$ m^2/s and an injection rate, $q = 10$L/min. Although this is a much lower injection rate than the average in Otaniemi there are also significant differences between the idealized boxcar injections used to produce Figure 11 and the much more complex schedule in Otaniemi. One can see that accounting for the role of delayed nucleation significantly widens the possible range of diffusivity in Otaniemi. Namely, the functional fit considers equally likely much higher values of c_{true} than would be predicted by the triggering front observed in Otaniemi given sufficient rate-and-state effects.

In light of this finding, we test the possibility that $c_{bu} = 0.044$ m^2/s is in fact closer to c_{true} in Otaniemi than c_{horner} as the inconsistency between the triggering front using $c_{bu} = c_{tf}$ and the relocated catalogue are borne due to rate-and-state effects. We test this hypothesis by finding the best fit of the rate-and-state model using $c_{bu} = c_{true}$. The effective radius and ambient pore pressure are adjusted to 31.1m and 54.9MPa, respectively, to best fit the well pressure measurements. The resulting fit for the seismicity rate in time is shown in Figure 6d, and the corresponding synthetic catalogue in space is shown in Figure 8d. a, $\dot{\tau}_r$, and r_b are found to be 0.00006, 1.29 kPa/yr and 4.7 events/day, respectively. The fit in time bears no significant improvement from the fit using $c_{horner} = c_{true}$, although the KS-statistic is slightly lower at 0.025. The fit in space is much improved with a higher mean of the distribution and cluster of events that encompasses greater portions of the relocated catalogue. One region the model performs rather poorly on is capturing the the back-propagation front starting around the 500-hour mark. It's possible that the back-propagation fronts, whose occurrence in time would correspond to the drawdown periods used for the Horner analysis, is still governed by the lower diffusivity c_{horner}. It could be that the back-propagation consists of two separate migration patterns, based on the observation that the initial portions of the back-propagation front are predicted quite well by the model (starting at around the 450-hour mark). This could be due to a propagation of the seismicity governed by different mechanisms than pore pressure diffusion, such as stress transfer by aseismic slip (Dublanchet & De Barros, 2021), although it is difficult to constrain the exact mechanism of seismicity migration given their possibly similar characteristics ($r \sim \sqrt{t}$).

The differences between c_{bu} and c_{horner} may be indications of distinct hydraulic processes that govern the well-head pressure and the spatial distribution of seismicity. One could imagine that the well-head pressure is more representative of the diffusivity of the medium immediately surrounding the well. On the other hand, the spatial distribution of seismicity may be more dependent on the path of highest hydraulic conductivity within the entire stimulated volume. The abrupt cessation of seismic activity close

to the injection well following shut-in could be associated to a decrease in the diffusivity due to fracture healing, leading to the lower estimate of c_{horner}. It is also important to note that the two diffusivities require different values of a, $\dot{\tau}_r$, and r_b, such that their independent measurements would provide stricter constraints on c_{true}. We see that the higher estimate c_{bu} inferred from this analysis yields synthetic catalogues in better agreement with the observed seismicity in time and space. We conclude using the triggering front to infer the diffusivity may yield a significantly biased estimate if the effect of earthquake nucleation is ignored.

7 Design of the Spatio-temporal Convolution Kernel

We now use the physical model as a basis to extend the temporal convolution model to space. We look for a new kernel with spatial dependence such that the convolution is as follows

$$R(t,x) = u(t) * g(t,x) = \int_{-\infty}^{\infty} u(\tau) g(t-\tau, x)\ d\tau \tag{12}$$

The spatial component of the kernel is constructed by using the half-norm distribution, as identified in Section 6, with a shape parameter increasing as $\sqrt{c_{hg}t}$. Combining with the Omori law as the temporal component as previously gives the integral of the kernel

$$\int_{-\infty}^{t} g(r,t')\ dt' = \frac{\sqrt{2}}{\sqrt{\pi c_{hg} t}} \exp\Big(-\frac{r^2}{2c_{hg}t}\Big) \cdot \Big(\frac{R_0}{1+t/t_r}\Big), \tag{13}$$

which is differentiated in time to obtain the response to Dirac forcing

$$g(r,t) = \frac{\sqrt{2}}{2\sqrt{\pi} t (c_{hg}t)^{3/2}} \exp\Big(-\frac{r^2}{2c_{hg}t}\Big) \cdot \frac{(-2c_{hg}t^2 - c_{hg}t(t+t_r) + r^2(t+t_r))R_0}{t_r(1+\frac{t}{t_r})^2} \tag{14}$$

The three parameters of the model are $c_{hg} = 0.011$ m^2/s, $R_0 = 213.5$ events/hr., and $t_r = 28.5$ hours, as estimated from the data. The fit to the temporal evolution of seismicity is, by design, identical to the fit obtained with the kernel in time introduced earlier (Figure 6a). The model provides now in addition a good match to the observations in space, especially with regards to the triggering and back-propagation fronts (Figure 8a). Overall, the convolution method approximates the physical model and fit the observations quite well, albeit with a drastically shorter computing time - by at least an order of magnitude - thanks to the use of the fast Fourier transform (the convolution is transformed into a simple product in the Fourier domain).

8 Discussion

8.1 Comparisons of Coulomb and Rate-and-State Models

Both rate-and-state and Mohr-Coulomb models are widely used in modelling induced seismicity. The standard Coulomb model assumes a population of faults with a uniform distribution of initial stress up to the maximum shear stress allowed by static friction (e.g., Ader et al, 2014). We show in supplement that this simplest version of the Coulomb model doesn't fit the observations neither in time nor in space (Text S4 and Figure S7). A number of studies which have tested the applicability of the Coulomb model to induced seismicity found it necessary to introduce a stress threshold that needs to be exceeded for earthquake triggering (e.g., Bourne et al., 2018; Dempsey & Suckale, 2017;

Dempsey & Riffault, 2019; Langenbruch & Shapiro, 2010; Rothert & Shapiro, 2003). The physical justification for the inclusion of the threshold, hereafter referred to as C_{cpt}, is to account for the population of faults activated during the stimulation that were initially in a relaxed state of stress, not close to failure. In this case, triggering would be delayed due to their initial strength excess rather than due to the nucleation process. The explanation is probably relevant in stable tectonic areas (e.g., Bourne et al., 2018; Dempsey & Suckale, 2017; Dempsey & Riffault, 2019; Langenbruch & Shapiro, 2010). Wenzel (2017) demonstrates the response of the Dieterich (1994) rate-and-state model, which assumes a population of faults above steady-state (initially already on their way to failure), can be approximated with such a threshold Coulomb model due to the tendency of $a\sigma$ to act as a stress threshold. On the other end, the application of the rate-and-state model to a population of faults below the steady-state regime also results in introducing a threshold in the rate-and-state model as well (Heimisson et al., 2022), accounting for the population of earthquake sources that are initially far from instability which is assumed negligible by Dieterich (1994). In this case, the question remains whether C_{cpt} is indeed solely representing the initial stress state, or rather acting as a proxy variable that also encompasses effects of time-dependent nucleation.

To address these questions, we consider a Coulomb model with a stress threshold representing the initial strength excess on the triggered faults. The Coulomb model is formulated as follows

$$R(t) = \frac{1}{\alpha_c} \int_V f_c\Big(p(r,t)\Big) \cdot \frac{\partial p}{\partial t}(r,t)\, dV, \tag{15}$$

$$\frac{\partial p}{\partial t}(r,t) = \frac{q(\lambda_u - \lambda)(\lambda + 2\mu)}{8\pi^{\frac{3}{2}}\rho_0 r^3 \alpha^2 (\lambda_u + 2\mu)} \xi^3 \exp\Big(-\frac{1}{4}\xi^2\Big), \tag{16}$$

where V is the representative volume over which seismicity is recorded, α_c is a scaling factor defined as the change in pore pressure per slip event per unit volume (Nur & Booker, 1972), and f_c is the probability density function representing the distribution of threshold triggering pressure needed for the Coulomb stress change to exceed the initial strength excess. Following the observation that poroelastic stress changes are minimal compared to pore pressure changes, they are ignored hereafter for simplicity. The derivation of equation (16), which is the time derivative of equation (7), is given in Appendix A of Segall & Lu (2015). The integral is restricted to where stress changes are positive, and to account for the Kaiser effect, the integral is further limited to where the past maximum pore pressure has been exceeded. Following Bourne et al (2018) and Smith et al. (2022), we next assume a population of faults with randomly distributed strength excess using a formulation that has been found to provide a good model of seismicity induced by gas extraction from the Groningen gas field. Seismicity starts once the Coulomb stress change exceeds the lowest value of the initial strength distribution. According to the extreme value theory, the tail of the distribution can be represented by a Generalized Pareto distribution, leading to an exponential increase of seismicity for a constant loading rate (Bourne et al., 2018). This general formulation is valid to simulate the onset of seismicity but it does not allow the transition to a steady state regime where seismicity rate would be proportional to the loading rate. We therefore assume a Gaussian distribution of initial strength to allow for the transition to steady-state (Smith et al., 2018), and express it in term of the distribution of threshold pressure

$$f_c(p) = \frac{1}{\theta_2\sqrt{2\pi}} \exp\left(-\frac{1}{2}\left(\frac{p-\theta_1}{\theta_2}\right)^2 \right), \tag{17}$$

where θ_1 and θ_2 are the mean and standard deviation of the distribution, respectively. The best fitting model is found with respect to θ_1 and θ_2 within the range of $0.01 \sim 5$

MPa for both parameters. α_c is adjusted to match the total number of events, much like r_b of the rate-and-state model. This model is hereafter referred to as the Coulomb model.

The model fit in time and space are shown in Figure 6e and 8e, respectively, with $\theta_1 = 0.66$ MPa, $\theta_2 = 0.28$ MPa, and $\alpha_c = 14.3$ kPa/event $\cdot$ m^3. The model fits the observations well in time, with a KS-statistic of 0.029 but significantly overestimates the extent of seismicity in space, which was also a main issue with the standard Coulomb failure mode (Supplementary Figure S7). The model is also less sensitive to rapid variations of the injection rate compared to the rate-and-state models, with relatively muted changes in the seismicity rate in-between injection cycles. Such sensitivity is seen to grow with the time scale of stressing rates; Figure 12 shows the response of the both the Coulomb and rate-and-state models with the duration of injections and pauses multiplied by factors of 0.1 and 10 (parameters are fixed to those that produced figures 6d&e). While both models show more rapid variations of the seismicity rate relative to the injection rate for longer injection duration, the tendency is significantly greater in the Coulomb model. For longer injection duration, the models show rather good agreement between each other although the Coulomb model predicts lower t_r with increasing time. Similar sensitivities may be observed with respect to the choice of θ_1. While both the Coulomb and rate-and-state models may provide sufficient hindcasting tools for the same observation, the calibrated models produce very different forecasts for injection scenarios with duration of injection different from those used for calibration. In addition, they may produce different predictions in space for similar predictions in time. The comparisons suggest that the stress state with respect to failure and nucleation effects must be modelled separately, as done for example in the threshold rate-and-state model of Heimisson et al. (2022), especially for fast injection cycles commonly employed in EGS operations where the effect of delayed nucleation may not be appropriately represented by the inclusion of a stress threshold in Coulomb models.

We remark that our modeling allows estimation of the best fitting values of a to between 0.00006 and 0.0002, which is significantly lower than the values inferred from laboratory measurements, generally ranging between 0.01 and 0.001 (Marone, 1998). Yet, the importance of rate-and-state effects in matching the observations in both space and time suggest that even such low values do not yield, for the injection schedule studied here, the rate-independent behavior that could be matched with a Coulomb model. The reconciliation of field-inferred values of $a\sigma$ and laboratory measurements is still paramount for eventual application of such models towards seismicity forecasting. One possible explanation is that spatial heterogeneities lead to elastic interactions that produce globally inferred values lower than that in a homogeneous equivalent (Dublanchet et al., 2013). It is also important to note that the model of Dieterich (1994) is a rather limited representation of the full complexity of rate-and-state friction. For example, the model simulates a population of spring-slider nucleation sources, whose qualitative differences in their behavior to more realistic finite fault models have been displayed for numerous aspects of rupture characteristics. Additionally, the model neglects the effect of variable effective normal stress on nucleation size, as the number of active nucleation sources remains constant throughout (Alghannam & Juanes, 2020). Further development of the model with a more holistic representation of rate-and-state friction would prove valuable for induced seismicity forecasting.

8.2 Origin of Omori-Law Decay Following Hydraulic Stimulation

The rate-and-state model reveals that the post shut-in Omori-law decay at Otaniemi depends strongly on the stress relaxation process by pore-fluid diffusion and cannot be explained solely by nucleation effects. The dependence on both nucleation and stress relaxation can be demonstrated by a sensitivity analysis of the relaxation timescale of the Omori law, t_r, to parameters a, the rate-and-state friction parameter and k, the permeability. We find the most direct relationship to be that between the ratios of t_r and the

characteristic diffusion time, $t_c = \frac{L^2}{c}$, to t_a as shown in Figure 13 where t_r is measured by fitting the Omori law to shut-ins following single boxcar injections under the rate-and-state model. Thus, t_r is more strongly dependent on t_c. The positive relationship t_r and t_c follows the intuitive reasoning that higher diffusivity would result in more rapid relaxation of induced pressure and consequently a faster decay of the seismicity rate. Our observations are consistent with the suggestion that the empirical Omori-law would be a result of stress relaxation by pore pressure diffusion (Almakari et al., 2019; Langenbruch & Shapiro, 2010; Miller, 2013). This explanation seems certainly reasonable in the context of EGS stimulations where pore pressure variations are particularly large.

The dependence on stress relaxation implies that t_r also depends on injection duration (Figure 13). where the sensitivity analysis is performed with a and k fixed at 0.001 and 10^{-16} m^2, respectively, while the injection duration varies between factors of 0.1 to 100 of t_c. The plot shows a non-linear relationship between t_r and the injection duration, t_I, with an initial increase followed by a decrease. The trend exhibits a strong correlation with the seismicity rate at the time of shut-in. For shorter injections, the seismicity rate continuously increases prior to shut-in, increasing the time to relax to background levels. This is until the seismicity rate begins to decrease for continued injection, as pore pressure reaches steady-state conditions, and further nucleation is suppressed by the Kaiser effect (Supplementary Figure S5). Consequently, t_r decreases as well, as it takes less time to relax the lower seismicity rate. A similar effect arises due to the finiteness of the computational domain – the further distances where the seismicity rate would continue to increase at later times are cut-off. The sensitivity of t_r to the total injected volume is consistent with the observation that the Omori law relaxation time at shut-in increases with time during the EGS stimulation at Otaniemi (Avouac et al., 2020).

8.3 Application of Models to Seismicity Forecasting

The models so far have only been applied in a hindcasting sense such that the data has been used in its entirety in order to tune the model parameters. We test the ability of the models to truly forecast induced seismicity in Otaniemi by limiting the range of the data used for training the models. Forecasts from the best fitting physical model (rate-and-state model with $c_{true} = c_{bu}$ - Figure 6d & 8d) and the spatio-temporal convolution model are shown in Figure 14 & 15, respectively. The rate-and-state model is able to produce a forecast comparable to the hindcast using just the first injection stage as the training period with a similar value of $a = 0.00005$ although with significantly lower $\dot{\tau}_r = 0.1$kPa/year and $r_b = 0.39$ events/day. With the same training period, the convolution model performs rather poorly, largely due to the estimation of t_r at the end of first injection stage substantially lower (2.9 hours) than the average value throughout the entire injection schedule. The forecast is significantly improved by including the second injection stage within the training period, which now consists of the Omori decay observed during the injection pause at around the 450-hour mark that significantly increases the estimated value of t_r to 10.4 hours.

It is likely that the rate-and-state model is more robust to the length of the training period than the convolution model due the fact that c_{true} is fixed at c_{bu} which matches the pressure history of Otaniemi in its entirety (Figure 7b). As discussed in Section 8.2, diffusivity plays a significantly stronger role in governing the rate of Omori decay than the tuning parameters of the rate-and-state model, namely a and $\dot{\tau}_r$. Thus, the rate-and-state model seems suited to perform well in forecasting applications given an accurate estimation of the diffusivity. Forecasts from the convolution model could also be improved by accounting for the increase in t_r with cumulative injected volume as observed in Otaniemi (Avouac et al., 2021).

8.4 Influence of the Kaiser Effect

We have seen that the fit to the temporal evolution of seismicity is improved when the Kaiser effect is reset at each new stimulation stage. Although the clouds of seismicity generated during each stimulation stage overlap largely (Figure 3), this reset is justified as each new stage implied the stimulation of a new volume near the wellbore. Without such an adaptation, the seismicity rate is predicted to significantly lower during the second half of the injection history (Figure 6c) along with large regions of seismic quiescence near the injection well (Figure 8c). This also implies that the efficacy of the convolution model - which does not account for the Kaiser effect at all - depends strongly on the apparent absence of the Kaiser effect in Otaniemi.

The physical mechanism behind the activation of new volumes is unclear given the diffuse and rather random structure of the relocated catalogue (Figure 3). If this argument is dismissed based on relocation uncertainties, one could pose that a low diffusivity stimulated non-overlapping volumes from one stage to the other. However, such a low diffusivity should manifest in inconsistencies with the observed catalogue in time, for instance a longer apparent relaxation time during shut-ins. Rather, the need to reset the stressing history for the models to reproduce the observations in Otaniemi more likely implies the creation of new hydraulic pathways due to the fracturing nature of the stimulation that activated new nucleation sources (Cladouhos et al., 2016). Such phenomenon would depend on both the physical properties of the injected medium such as its fluid transport properties and fracture toughness, and the injection scenario, especially any spatial variation of the injection location.

8.5 Validity of the Convolution Model

Our study show that, in the context of the Otaniemi injection schedule, the seismicity response to injections in time and space can be approximated with a simple convolution model. This model ignores all the sources of non linearity that may arise from the coupling between fluid flow and deformation, the earthquake nucleation process, the initial strength distribution and Kaiser effect. It is therefore not obvious that this approximation would be applicable to other induced seismicity context or for other injection schedules. We have therefore used our physical model to explore the parameter regimes under which the the linear convolution method is able to match the rate-and-state model. The results are presented in the Supplementary Text S6. We found the success of the convolution model to depend strongly on the impact of the Kaiser effect on the linearity of stress evolution for the given injection schedule although it is also seen to be robust to non-linear effects from delayed nucleation.

9 Conclusion

Physical models based on rate-and-state friction and stress changes due to pore-pressure diffusion and poroelasticity can successfully reproduce the seismicity observed during the EGS simulation which were carried out on the Otaniemi campus near Helsinki, Finland. While pore pressure measurements at the well indicate two possible diffusivities that fit either the build-up of pressure or its drawdown, the physical model suggests that the diffusivity of the medium is likely closer to the higher diffusivity fitting the build-up. We find that the effect of time-dependent nucleation is crucial in reconciling the higher diffusivity with the spatio-temporal distribution of triggered seismicity. Namely, the tendency of the parameter $a\sigma$ to act proportionally to a triggering threshold significantly affects the apparent diffusivity inferred from the triggering front in Otaniemi. However, the effect of nucleation cannot be approximated well by introducing a stress threshold in the standard Coulomb friction model, at least in the context of rapid variations of injection rates common in EGS operations. We remark that there are significant portions of the relocated catalogue that the models do not fully capture in space, such as the back-

propagation front or far-field seismicity, although a significant portion of the observed far-field seismicity may have been due to leaks in the well casing. The Omori law decay observed in Otaniemi is seen to depend strongly on fluid transport properties in the physical model. Lastly, the physical model indicates that the Kaiser effect is present in Otaniemi, weakened by the successive variation of injection locations between different stages.

We show that a statistical model whereby the seismicity rate is predicted in time and space by convolution of a kernel function inspired by Omori law decay with the injection rate can provide a good match to the seismicity observed in Otaniemi. The existence of such linear convolution kernels is consistent with the identification of systematic decay patterns in the rate densities calculated by adaptation of the cascading algorithm of Marsan & Lengline (2008) to induced seismicity. The statistical model is extended to space by incorporation of a half-norm distribution component to the kernel mimicking the behavior of the physical model. We find that the validity of the method, which assumes a linear relationship between the injection history and the induced seismicity rate, depends strongly on the presence of the Kaiser effect. The convolution model would be applicable towards injection schedules that minimize the impact of the Kaiser effect by decreasing injection durations relative to the local diffusion time or by variation of injection locations in space.

The physical model presented in this study makes a number of assumptions. One assumption is that it is appropriate to use Darcy's Law, which was established for a homogeneous porous medium, to model the flow in the fractured crystalline bedrock. Although the assumptions largely stem from the lack of data on local heterogeneities or anisotropy, neglecting presence of vertical or horizontal geological layers may be appropriate for Otaniemi where the objective is to fracture a largely crystalline medium. The model also ignores the effect of pore-pressure change on permeability. This is clearly an oversimplification as, in the case of fractured flow, the permeability increases substantially with pore pressure (Acosta & Violay, 2019; Cappa et al., 2014; Cornet & Jianmin, 1995; Evans et al., 2005). Common values of in-tact granite under comparable pressure are documented to be closer to 10^{-21} m^2 (Brace, Walsh & Frangos, 1968), several orders of magnitude lower than that of the best fitting model (10^{-16} m^2). Indeed, there are indications of changes in the diffusivity from the evolution of the injectivity index, or the ratio of injection rate to the well-head pressure (Supplementary Figure S10). Periods of heightened injectivity are well-correlated with periods of high seismicity rates, likely due to seismicity-induced increase in permeability. Reconciling the full scope of pressure variations at the well and the spatio-temporal patterns of observed seismicity would probably require an explicit account for the role of fractures and seismicity on permeability. Lastly, stress perturbations due to thermoelasticity can also be significant for EGS operations where temperature gradients between the injected fluid and surrounding medium are large (e.g., Gens et al., 2007; Rutqvist & Oldenburg, 2008; Im et al., 2017).

The modeling methods presented here could be useful in designing EGS operations or to interpret induced seismicity observations in terms of transport properties within the stimulated volume. They could additionally serve as a basis for a probabilistic traffic light system (TLS) or be incorporated in a control and optimization framework such as the one presented by Stefanou (2019). At the moment, TLS are deterministic and based entirely on the observed maximum magnitude (Ader et al. 2020; Bommer et al. 2006; Kwiatek et al., 2019; Majer et al. 2007). As such, a red light event can be triggered by the occurrence of a rare event, with improbably large magnitude, that might not necessarily reflect an increased hazard level. In addition, such TLS don't provide a way to anticipate the response to possible mitigation strategies. This is important as many operations have been terminated as the original TLS design proved to be insufficient in preventing "red-light" incurring events (Grigoli et al., 2017; Majer et al. 2007). To alleviate that issue, our forecasting methods could for example be incorporated in "Adaptive

Traffic Light Systems" (ATLS) (Wiemer et al., 2015), which are based in a real-time assessment of probabilistic hazard.

Parameter	Variable	Value and Unit
Poroelastic Properties		
Shear Modulus	μ	20 GPa
Drained Poisson's Ratio	ν	0.25
Undrained Poisson's Ratio	ν_u	0.3
Skempton's Coefficient	B	0.75
Biot's Coefficient	α	0.31
Transport Properties		
Fluid Viscosity	η	0.4×10^{-3} Pa·s
Reference Fluid Density	ρ_0	10^3 kg/m^3
Normal Stress	σ	155 MPa
Frictional Properties & Fault Orientation		
Fault Normal	$\hat{n}$	[-0.866, 0, 0.5]
Fault Slip	$\hat{s}$	[-0.5, 0,-0.866]

Table 1: Constant Parameters

811 [t] [t]

Figure #	Parameters				KS-statistic		LLK
					Time	Space	Time
	Convolution Model						
	c_{hg} [m²/s]		t_r [hours]	R_0 [events/hour]			
6a & 7a	0.011		24.1	208.9	0.040	0.122	176558
	Rate-and-State Model						
	c_{true} [m²/s]	a	$\dot{\tau}_r$ [kPa/year]	r_b [events/day]			
6b & 7b	0.018	0.0002	3.05	12.1	0.029	0.335	173375
6c & 7c	0.018	0.0001	4.89	25.9	0.090	0.136	165532
6d & 7d	0.044	0.00006	1.29	4.7	0.025	0.110	173429
	Coulomb Model with Gaussian Threshold						
	c_{true} [m²/s]	θ_1 [MPa]	θ_2 [MPa]	α_c [kPa/event•m³]			
6e & 7e	0.044	0.66	0.28	14.3	0.029	0.392	173035

Table 2: Model Parameters

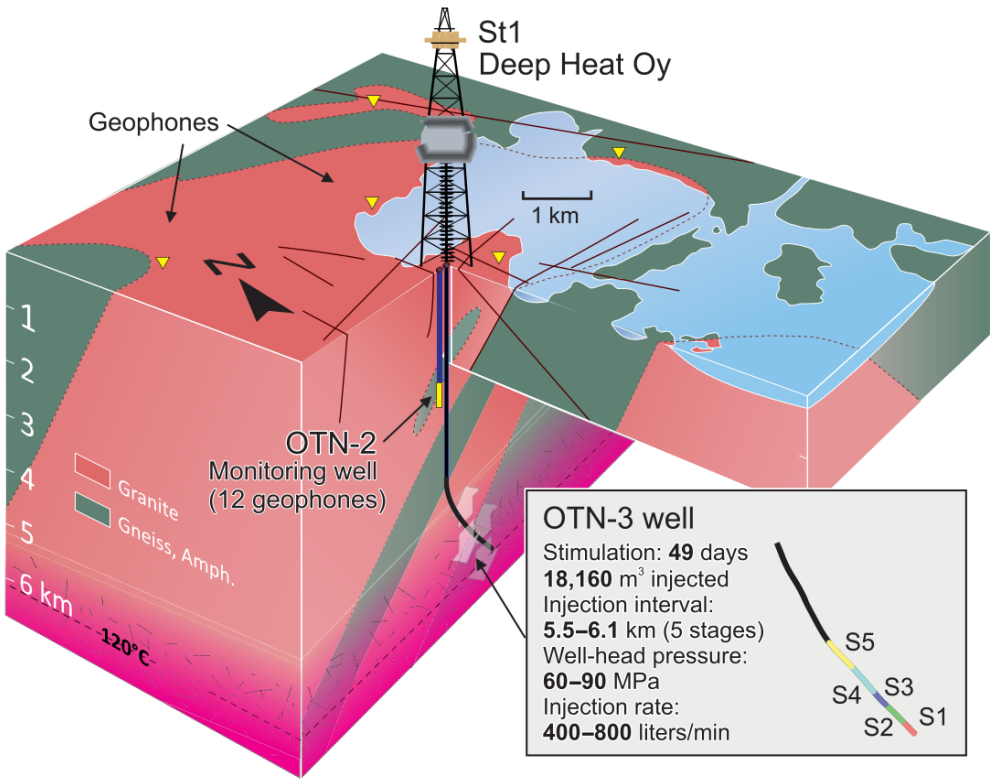

Figure 1: Well-Stimulation Operation in Otaniemi, Finland (Kwiatek et al., 2018): The observation well (OTN-2) and stimulation well (OTN-3) are indicated by lines extending into depth at the center of the schematic. Locations of various geophones within the area are indicated by the yellow triangles. Locations of stimulation stages S1 to S5 vary along OTN-3. Basic stimulation parameters are shown in the inset.

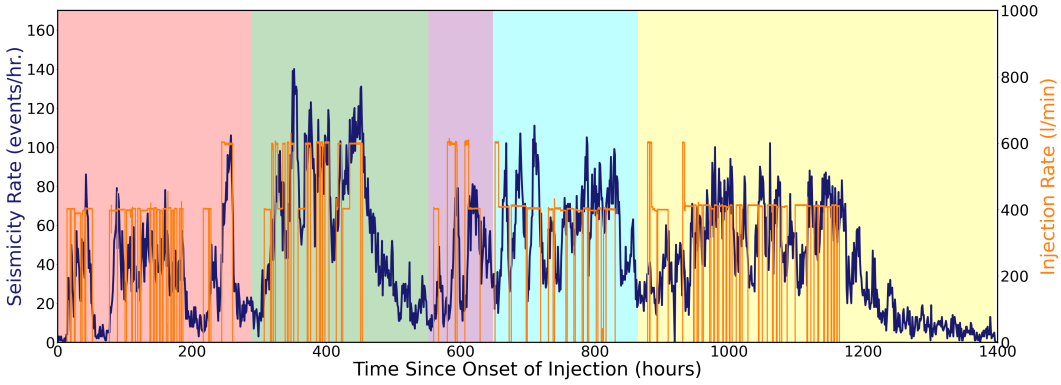

Figure 2: Earthquake Catalogue in Otaniemi: The complete catalogue of Leonhardt et al. (2021) is plotted in dark blue as a histogram. The injection rate history is plotted in orange. The background colors represent the timing of the individual injection stages. The seismicity rate shows a strong positive correlation to the injection rate.

812 [t]

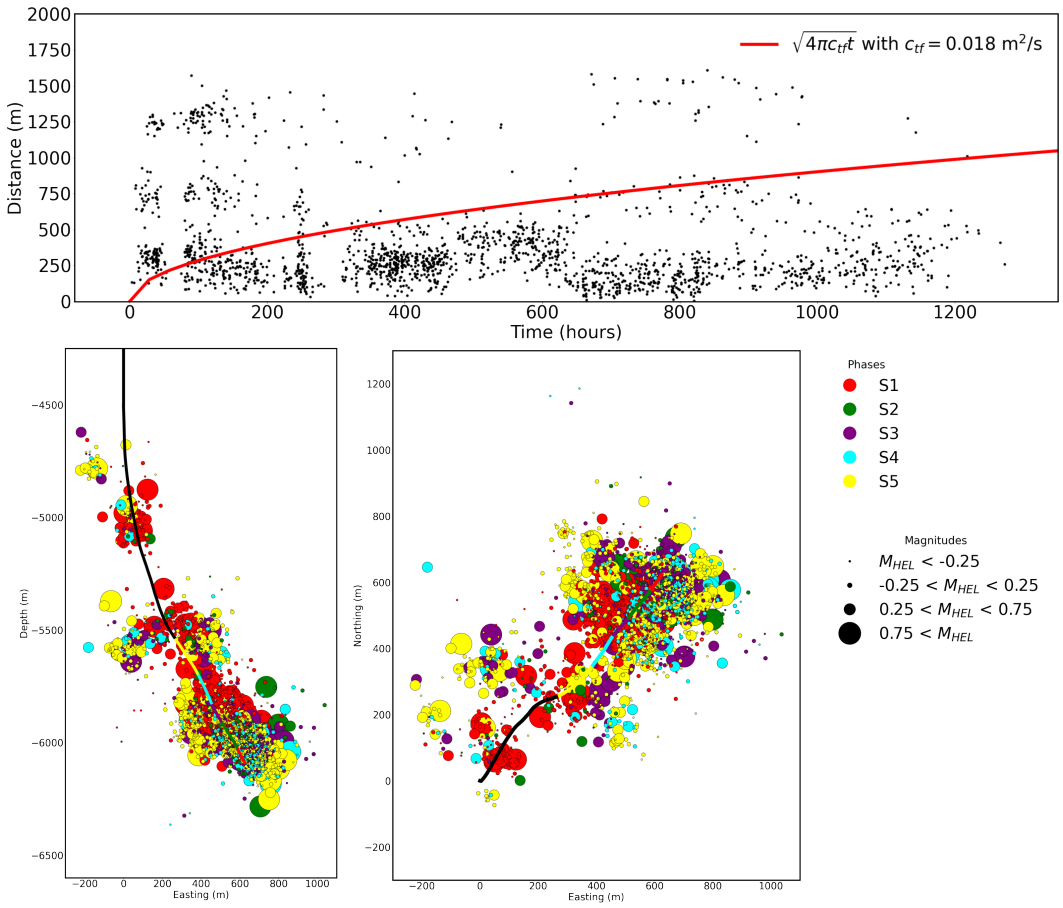

Figure 3: Relocated Catalogue of Leonhardt et al. (2021): 1986 relocated events are indicated as black dots according to their distances from the injection source and time of occurrence (top). The red curve outlines the theoretical triggering front of Shapiro (1997), $\sqrt{4\pi c_{tf} t}$, with $c_{tf} = c_{horner} = 0.018$ m^2/s. It is difficult to assess a level of agreement between the triggering front and the relocated catalogue given the limited sample size. Yet, clusters of events far beyond the curve suggest poroelastic triggering. It is also possible that they are due to leaks in the casing, as evidenced by their locations close to the well path shown in the vertical section view (bottom-left). In the map (bottom-right) and and vertical section views, the well is drawn in black with stimulated sections of the well and occurrence time of events color-coded correspondingly. M_{HEL} refers to the local Helsinki magnitude scale. The color-coding reveals little correlation in space between events and stimulation stages.

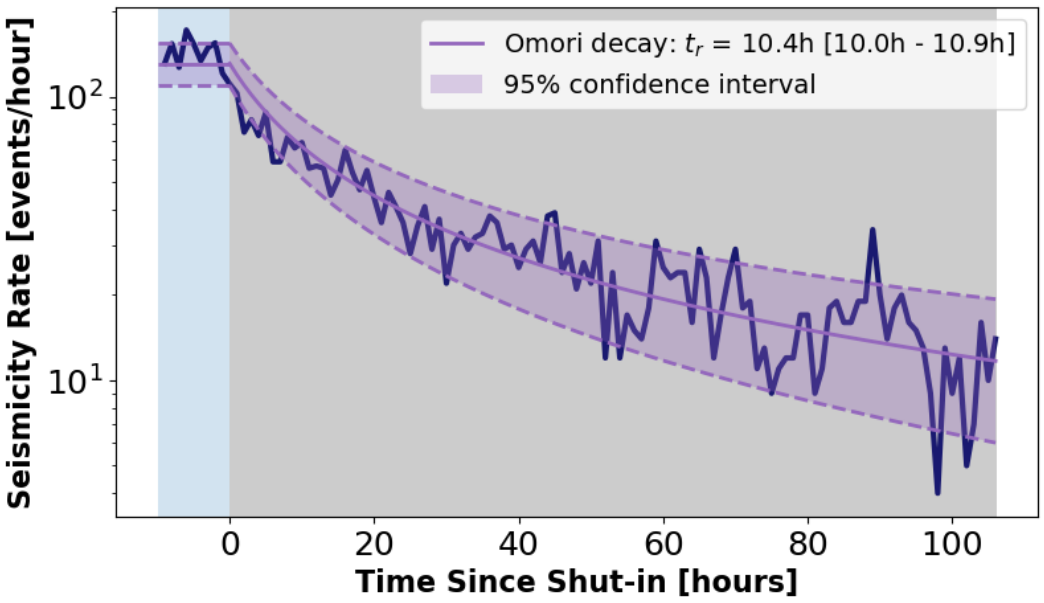

Figure 4: Omori Law (p=1) Decay During Shut-in: The recorded catalogue in time is zoomed-in on an interval during which injection has largely stopped (around 450-hour mark in Figure 2). A Short period prior to shut-in is shown with a sky blue background. The shut-in period is indicated with a grey background. The decay pattern in seismicity rate during the shut-in is matched well with an Omori decay function (modified Omor-Utsu law with p=1), plotted in light purple. The dotted lines and shaded areas in-between indicate the 95% confidence interval of the fit. The fitted value of t_r and the bounds of the confidence interval of the fit are indicated in the legend.

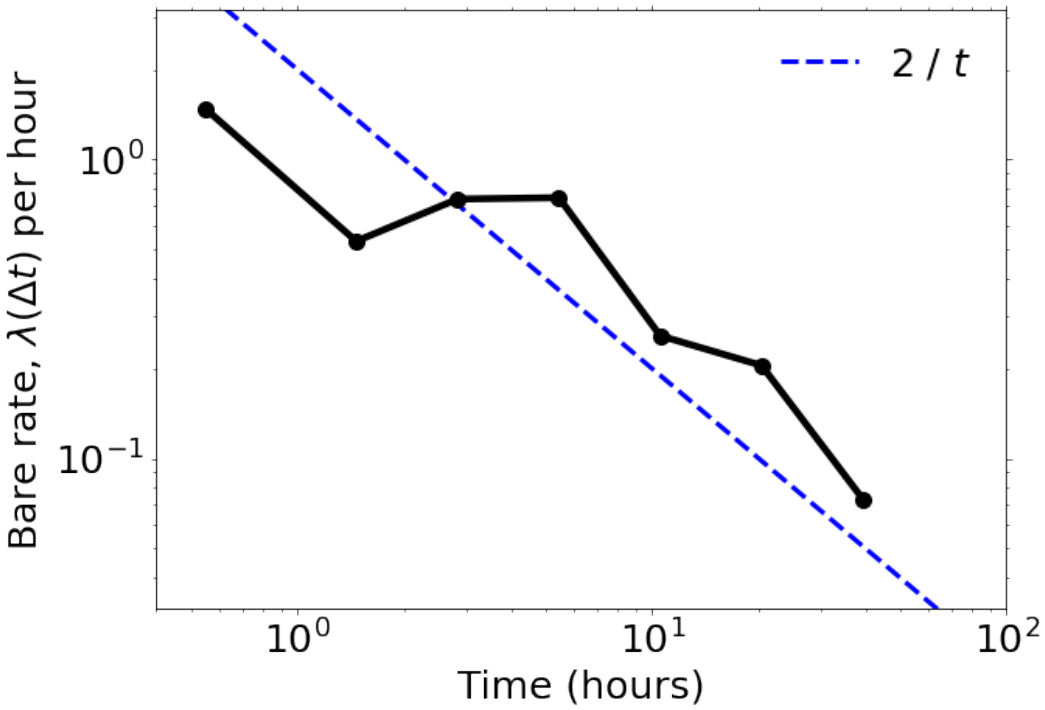

Figure 5: Marsan & Lengline (2008) Rate Densities: Rate densities measuring the weight of influence from individual injections onto induced events are computed through an adaptation of the cascading algorithm from Marsan & Lengline (2008). The densities follow a $1/t$ type of decay in time, consistent with the Omori-law decay observed during shut-ins (Figure 4) and suggestive of the possibility for a convolution kernel relating injections to induced seismicity.

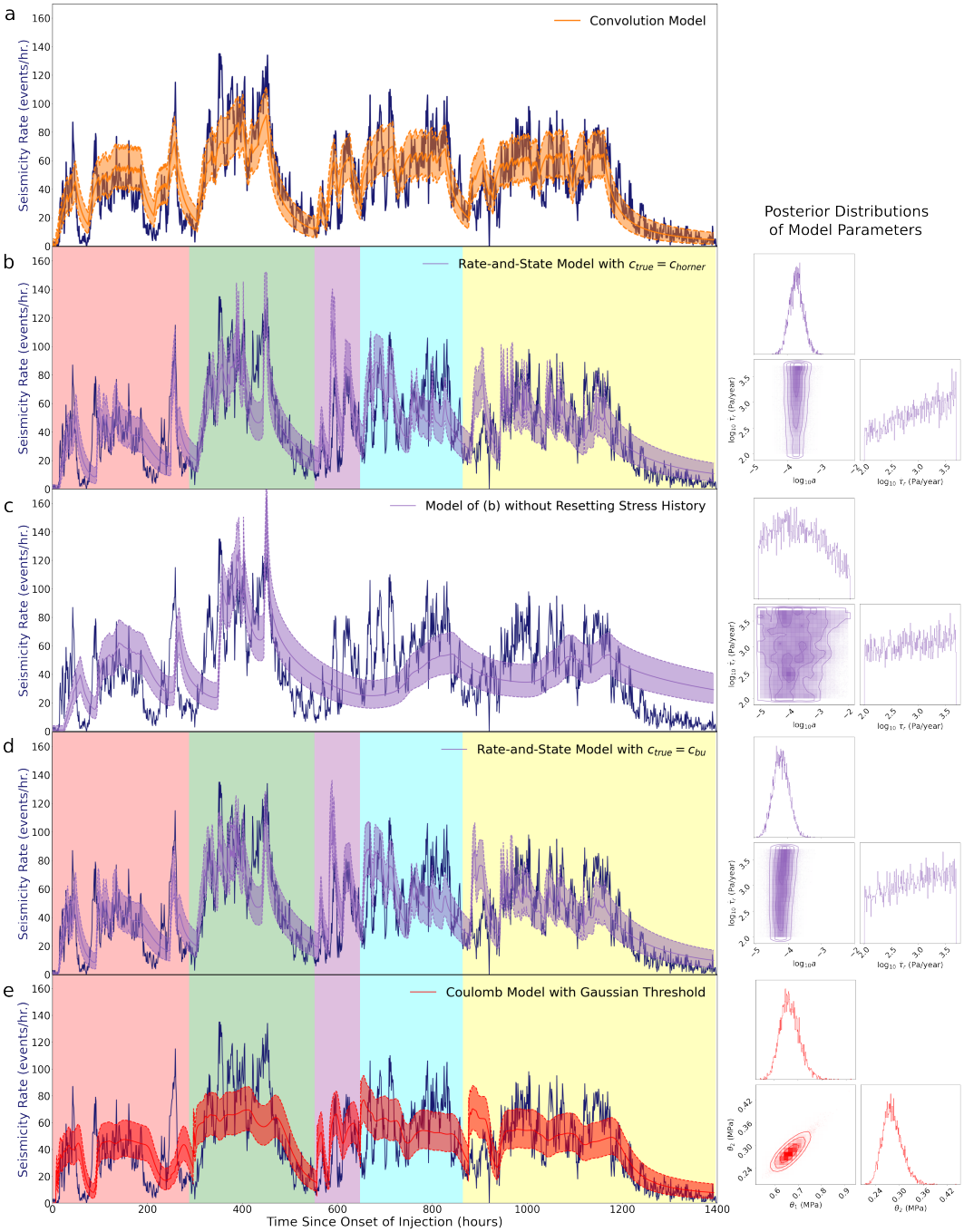
a
Convolution Model
b
Rate-and-State Model with $c_{true} = c_{horner}$
c
Model of (b) without Resetting Stress History
d
Rate-and-State Model with $c_{true} = c_{bu}$
e
Coulomb Model with Gaussian Threshold
Seismicity Rate (events/hr.)
Time Since Onset of Injection (hours)
Posterior Distributions of Model Parameters
$\log_{10} a$
$\log_{10} \tau_r$ (Pa/year)
θ_1 (MPa)
θ_2 (MPa)

Figure 6:

Figure 6: Model Predictions in Time: Model predictions are plotted in different colored shading over the observed catalogue in dark blue. The dotted-lines and shaded areas in-between indicate the 95% confidence interval of the prediction. Posterior distributions of fitted parameters are shown on the right for applicable models. Rest of the parameters are as listed in Table 1. a) Linear convolution of the injection history with t_r = 24.1 hours and r_b = 208.9 events/hr. (b) Rate-and-state model with $c_{true} = c_{horner}$ = 0.018m^2/s, $a = 0.0002$, $\dot{\tau}_r = 3.05$ kPa/year and $r_b = 12.1$ events/day. (c) Rate-and-state model without resetting of stress history with $a = 0.0001$, $\dot{\tau}_r = 4.89$ kPa/year and r_b = 25.9 events/day performs progressively worse with significant lags during the latter half, largely due to the Kaiser effect inherent in the rate-and-state model (Figure S5). (d) Rate-and-state model with $c_{true} = c_{bu} = 0.044\text{m}^2$/s, $a = 0.00006$, $\dot{\tau}_r = 1.29$ kPa/year and $r_b = 4.7$ events/day. (e) Coulomb model with $c_{true} = c_{bu} = 0.044$ m^2/s, $\theta_1 = 0.66$ MPa, $\theta_2 = 0.28$ MPa, and $\alpha_c = 14.3$ kPa/event $\cdot$ m^3. While the global fit to the observations are comparable to other models, it lacks rapid variations of the seismicity rate in-between injection cycles compared to the rate-and-state models - evident of qualitative differences in modelling the stress state relative to failure and delayed nucleation mechanisms. All models (besides (c)) consistently capture temporal trends of the seismicity rate, such as the Omori-law decay during shut-ins and build-up periods at the onset of injections, with the linear convolution model requiring the fewest parameters and lowest computational cost. Model parameters and goodness-of-fit metrics are summarized in Table 2.

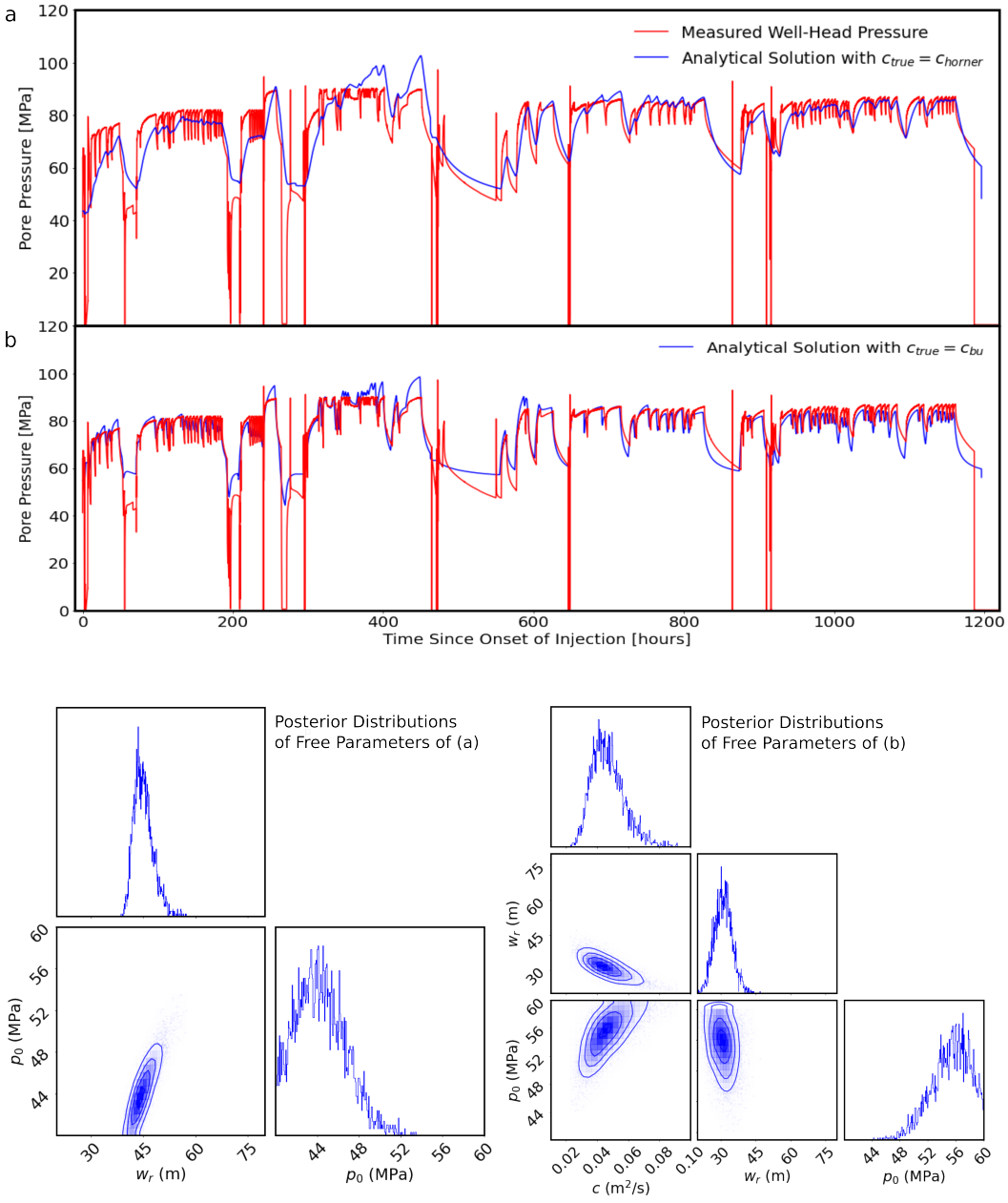

Figure 7: Well-Pressure Measurements and Modelled Fit: Observed well-pressure and the modelled fits are plotted in red and blue, respectively. The top fit corresponds to $c_{true} = c_{horner} = 0.018$ m^2/s, effective well radius, w_r, of 44m and ambient pore pressure, p_0, of 43.5 MPa while the bottom fit corresponds to $c_{true} = c_{bu} = 0.044$ m^2/s, $w_r = 31$m and $p_0 = 54.9$ MPa. The posterior distributions of w_r and p_0 for $c_{true} = c_{horner}$ are shown on the bottom-left and those for c_{bu}, w_r and p_0 are shown on the bottom-right. While both models provide a good global fit to the data, c_{horner} and c_{bu} tend to fit better either the drawdown of pressure during shut-ins or the build-up of pressure at injection onsets, respectively.

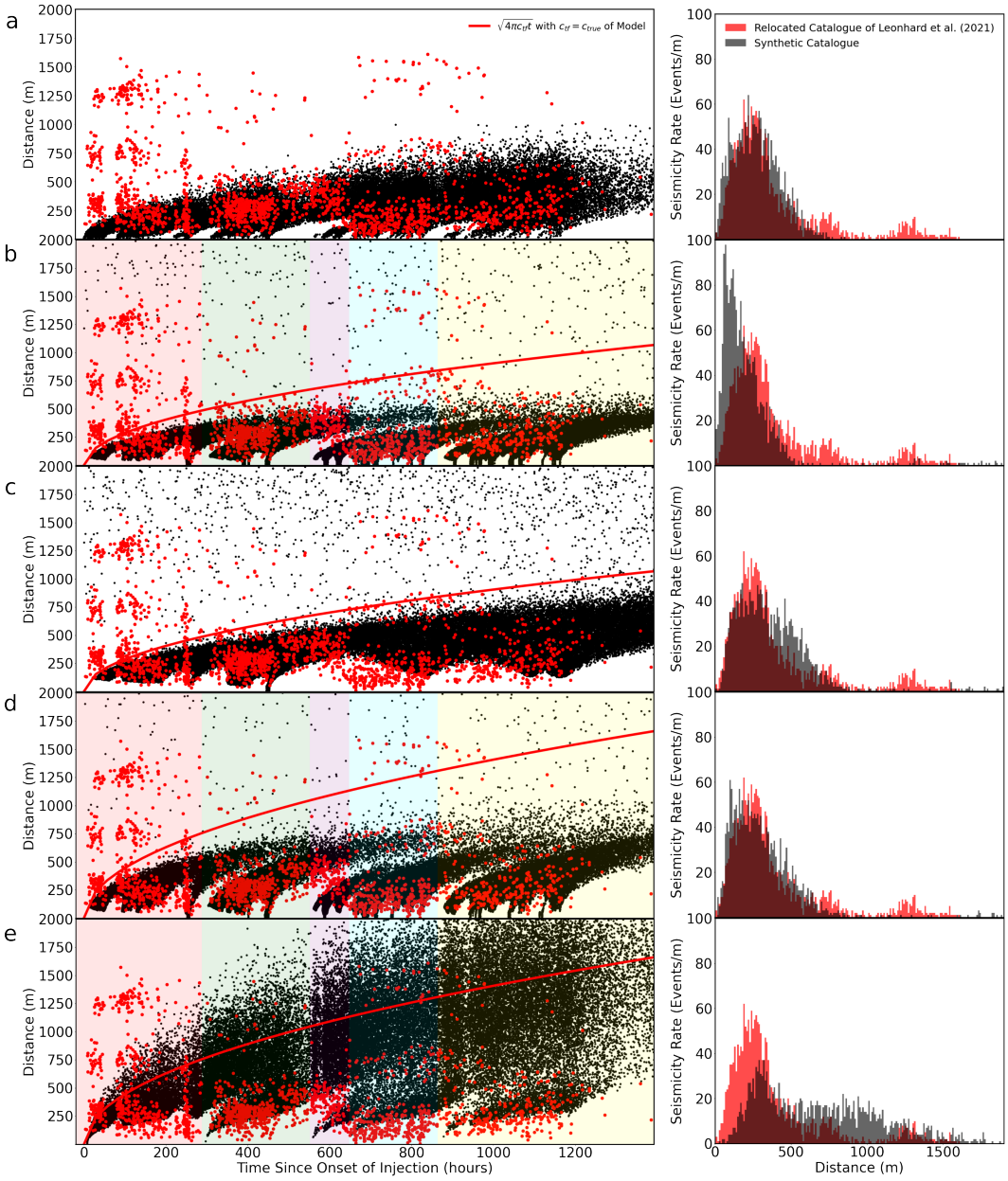
a
b
c
d
e
Distance (m)
Time Since Onset of Injection (hours)
$\sqrt{4\pi c_{tf} t}$ with $c_{tf} = c_{true}$ of Model
Relocated Catalogue of Leonhard et al. (2021)
Synthetic Catalogue
Seismicity Rate (Events/m)
Distance (m)

Figure 8:

Figure 8: Model Predictions in Space: The synthetic catalogue is plotted as black dots in space and time with the relocated catalogue of Leonhardt et al. (2021) superposed as red dots. The red curve outlines $\sqrt{4\pi c_{tf} t}$ with $c_{tf} = c_{true}$ for each model. Histograms of the observed event distribution in space is plotted in red along with randomly sampled distributions of the synthetic catalogues in black. (a) The extension of the convolution model to space gives a good fit to the observations using the estimate of $c_{hg} = 0.011$ m^2/s. (b) The rate-and-state model with $c_{true} = c_{horner} = 0.018$ m^2/s underpredicts the mean distance substantially with an apparent triggering front much closer to the injection source. (c) Rate-and-state model without resetting of stress history with $a = 0.0001$, $\dot{\tau}_r$ = 4.89 kPa/year and $r_b = 25.9$ events/day shows manifestations of the Kaiser effect from large regions of seismic quiescence in stress shadows near the injection source. (d) The fit to space in the rate-and-state model is significantly improved with $c_{true} = c_{bu} = 0.044$ m^2/s. The rate-and-state models consist of far-field seismic activity, although mostly from background stressing distributed uniformly in space rather than through a systematic variation from poroelastic stress perturbations. (e) The Coulomb model with $c_{true} = c_{bu}$ = 0.044 m^2/s significantly overpredicts the distribution of seismicity in space as does the theoretical triggering front for $c_{tf} = c_{bu}$, suggesting that the role of delayed nucleation on seismicity migration is essential in reproducing the observed spatio-temporal evolution of seismicity in Otaniemi given the likely diffusivities. Model parameters and goodness-of-fit metrics are summarized in Table 2.

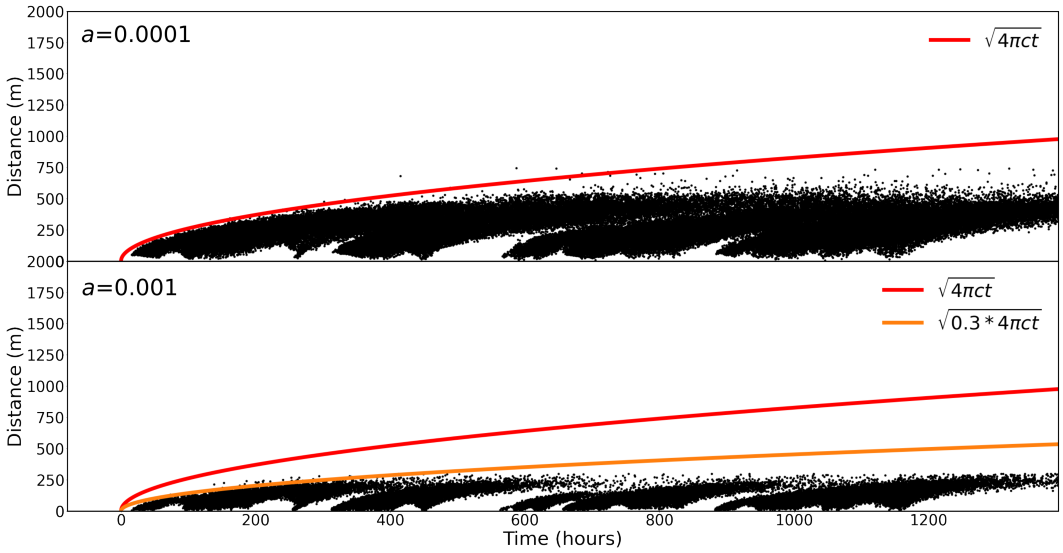

Figure 9: Sensitivity of Triggering Front to Delayed Nucleation: Synthetic catalogues for two parameter sets only differing by a (0.0001 and 0.001 in top and bottom, respectively) are shown. Lower a, which translates to lower $a\sigma$, results in a much further extent of the triggering front, due to the role of delayed nucleation that acts proportionally to a threshold stress for the triggering of events as explained in detail by (Wenzel, 2017). Along with the reference triggering front in red, an additional $\sqrt{4\pi c_{tf} t}$ curve is drawn in orange for a = 0.001, with c_{tf} modified by a factor of 0.3 that better matches the apparent triggering front.

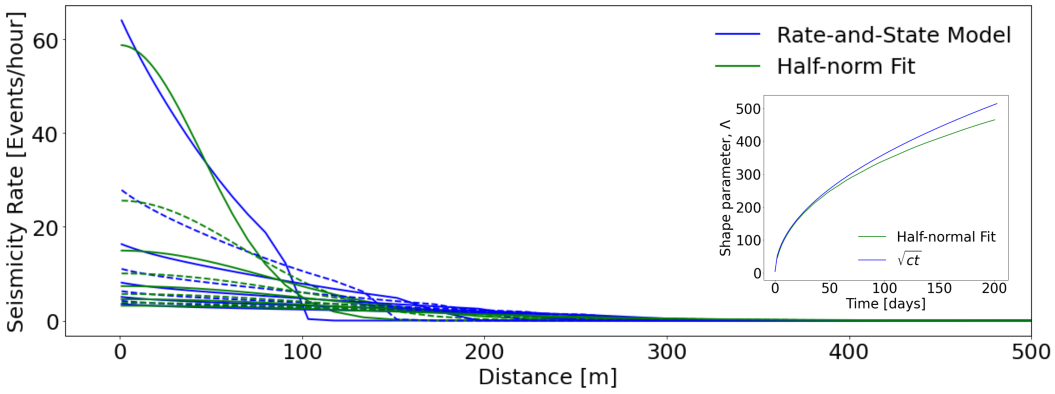

Figure 10: Evolution of Spatial Distribution of Seismicity for Rate-and-State Model: Spatial profiles of the seismicity rate are plotted in blue at various times for the rate-and-state model in response to a single boxcar injection. Half-norm distributions, in green, are used to fit the model-generated distribution. The line style is alternated between solid and dashed between each time step for clarity. The half-norm distributions evolve with a time-dependent shape parameter, $\Lambda(t)$, which closely follows $\sqrt{c_{true}t}$ as shown in the inset of the top figure.

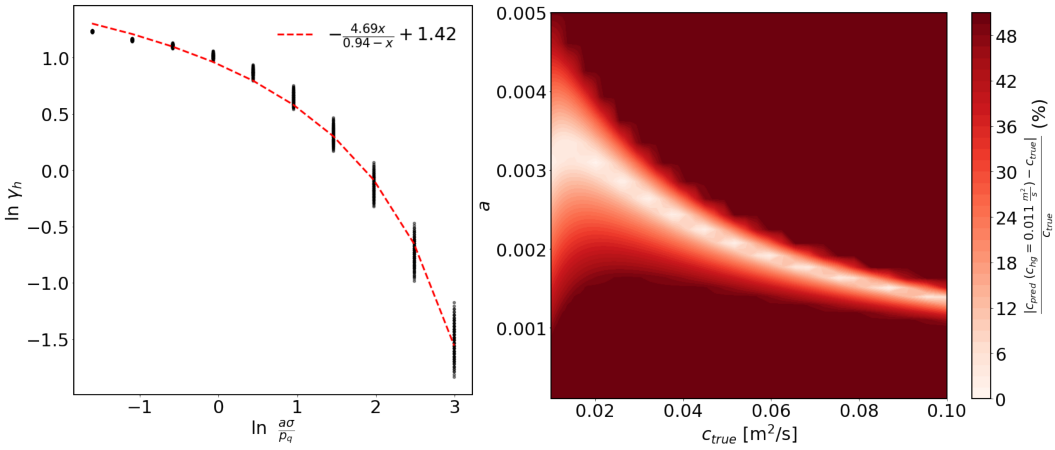

Figure 11: Inference of Diffusivity Accounting for Role of Delayed Nucleation on Seismicity Migration: An empirical relationship for the multiplicative factor, γ_h, of $\Lambda(t) = \sqrt{\gamma_h c_{true} t}$ is found in terms of the non-dimensional ratio $a\sigma/p_q$ (left). The fit can be used to infer new uncertainty estimates on the diffusivity of the medium given apparent spreading of the radial distribution of the seismicity in Otaniemi, i.e. $c_{hg} = 0.011$ m^2/s. Contour plot on the right shows the percent difference between the true diffusivity and the predicted diffusivity from the functional fit $\gamma_h(a\sigma/p_q)$ for a range of a and c_{true}. Considerations of the role of delayed nucleation on seismicity migration makes higher diffusivities more likely than previously considering solely the theoretical triggering front of Shapiro (1997).

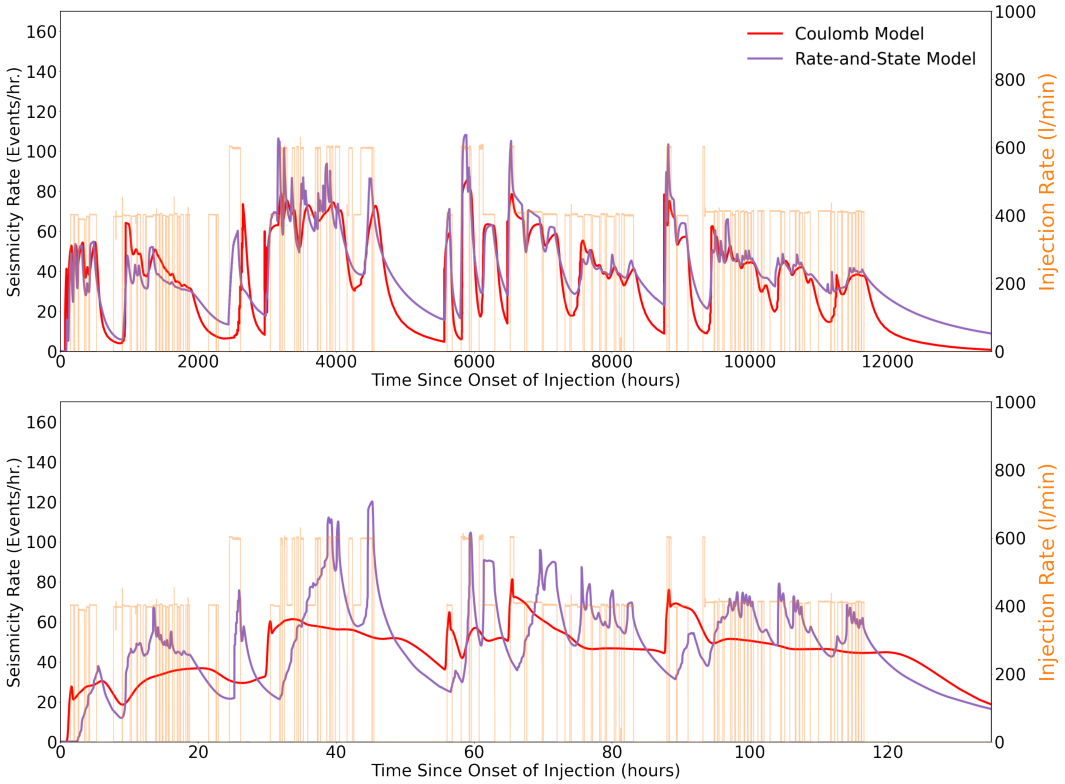

Figure 12: Comparison of Rate-and-State and Coulomb Model For Varying Time Scale of Injections: The rate-and-state and coulomb models that produced best fitting predictions of Figure 6d&e, respectively, are compared in their response to the injection scenario of Otaniemi with injection durations lengthened (top) and shortened (bottom) by 10 times. The injection rate is shown in light orange. The Coulomb model shows significant disagreement with the rate-and-state model for shorter injections, illustrating the differences in modelling the stress state with respect to failure and delayed nucleation at shorter time scales.

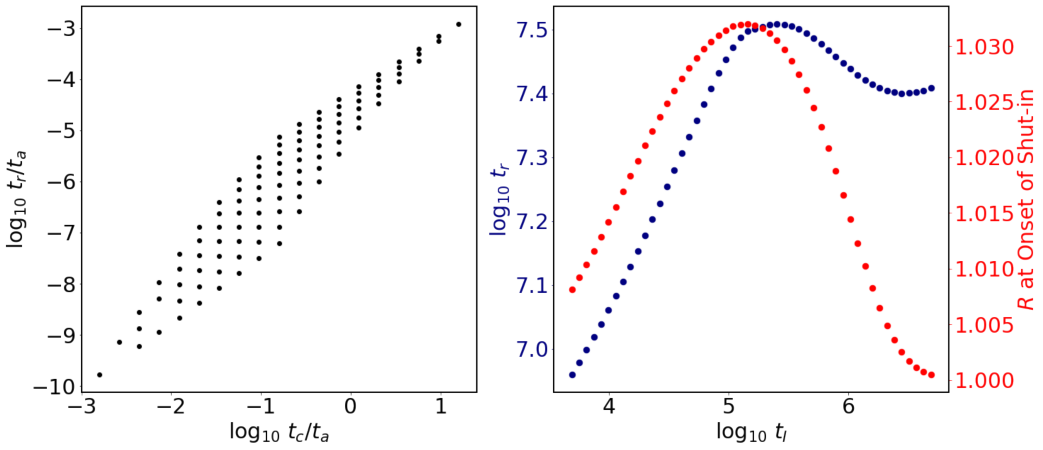

Figure 13: Dependence of Omori Law Decay on Fluid Transport Properties: t_r of Omori Law Decay in response to single boxcar injections under the rate-and-state model are plotted in terms of t_c and t_a (left). t_r, shows a stronger dependence on t_c, or the diffusivity, than on t_a. Namely, longer diffusion times result in longer relaxation times of the seismicity rate. t_r also shows strong dependence on injection duration, t_I (right). t_r first increases with increasing seismicity rate at time of shut-in, before decreasing as steady-state stress conditions are reached when the seismicity rate decreases as well due to the Kaiser effect (Supplementary Figure S5).

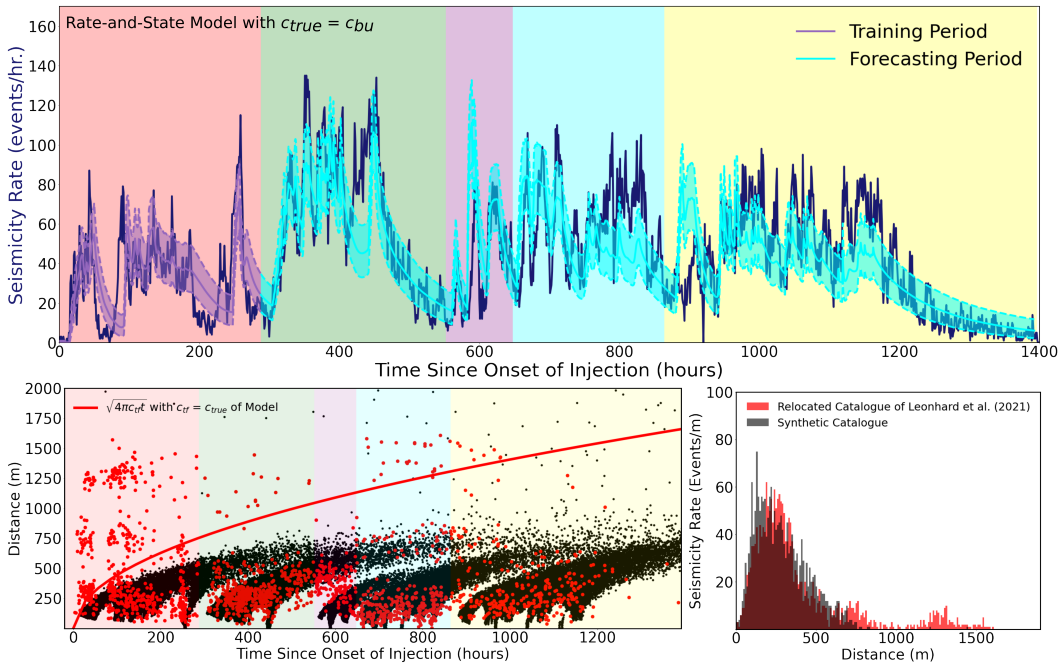

Figure 14: Partial Forecasting of Induced Seismicity by Physical Model: Ability of the physical model to forecast induced seismicity is tested by limiting the portion of the data used for model tuning. The rate-and-state model with $c_{true} = c_{bu} = 0.044$ m^2/s is trained using only the first injection stage. The training results in a, $\dot{\tau}_r$, and r_b of 0.00005, 0.1kPa/year, and 0.39 events/day. The forecast is comparable to the hindcast of Figure 6d & 8d, with only a marginally higher KS-statistic of 0.040 and lower log-likelihood of 169,076.

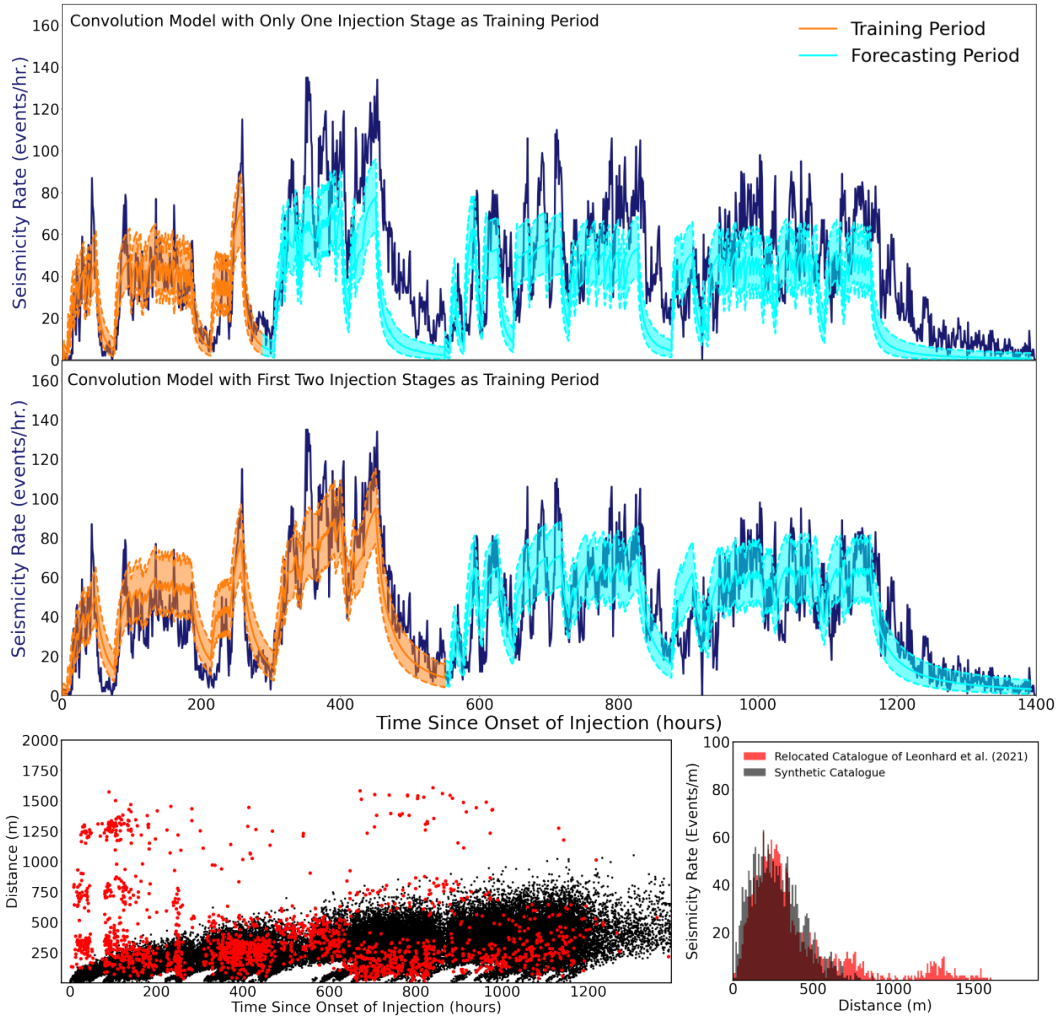

Figure 15: Partial Forecasting of Induced Seismicity by Convolution Model: Ability of the convolution model to forecast induced seismicity is tested by limiting the portion of the data used for model tuning. The top two rows compare forecasts using the first one and two injection stages as training periods where t_r is estimated to be 2.9 and 10.4 hours, respectively. The forecast using solely the first injection stage as the training period significantly underestimates t_r and underpredicts the seismicity rate for the rest of the injection history. The forecast using the first two injection stages as the training period is comparable to the hindcast of Figure 6a & 8a, with only a marginally higher KS-statistic of 0.047 and lower log-likelihood of 175,430.

Acknowledgments

This study was supported by the National Science Foundation via the Industry-University Collaborative Research Center Geomechanics and Mitigation of Geohazards (award #1822214) and the National Science Foundation Graduate Research Fellowship (award #DGE-1745301). The authors are grateful to Dr. David Dempsey and the associate editor for their insightful and thorough reviews. We would like to thank our colleagues and collaborators for numerous discussions and their comments on the manuscript, in particular Grzegorz Kwiatek, Mateo Acosta, Kyungjae Im, Krittanon Sirorattanakul, Maxim Vraine, Guanli Wang, Thomas Ader, and Tero Saarno.

10 Data Availability Statement

The seismic data used in this paper are available from Leonhardt et al. (2021) via https://doi.org/10.5880/GFZ.4.2.2021.001. Scripts used for the convolution model, physical models, diffusivity inference from well pressure analysis and MCMC inversions are available at https://doi.org/10.5281/zenodo.7246648.

References

Acosta, M., & Violay, M. (2020). Mechanical and hydraulic transport properties of transverse-isotropic gneiss deformed under deep reservoir stress and pressure conditions. *International Journal of Rock Mechanics and Mining Sciences*, *130*(10423), 5.

Ader, T., Chendorain, M., Free, M., Saarno, T., Heikkinen, P., Malin, P. E., & Vuorinen, T. (2020). Design and implementation of a traffic light system for deep geothermal well stimulation in finland. *Journal of Seismology*, *24*(5), 991-1014.

Ader, T. J., Lapusta, N., Avouac, J. P., & Ampuero, J. P. (2014). Response of rate-and-state seismogenic faults to harmonic shear-stress perturbations. *Geophysical Journal International*, *198*(1), 385-413.

Aki, K., Fehler, M., Aamodt, R. L., Albright, J. N., Potter, R. M., Pearson, C. M., & Tester, J. W. (1982). Interpretation of seismic data from hydraulic fracturing experiments at the fenton hill, new mexico, hot dry rock geothermal site. *Journal of Geophysical Research: Solid Earth*, *87*, 936-944.

Alghannam, M., & Juanes, R. (2020). Understanding rate effects in injection-induced earthquakes. *Nature communications*, *11*(1), 1-6.

Almakari, M., Dublanchet, P., Chauris, H., & Pellet, F. (2019). Effect of the injection scenario on the rate and magnitude content of injection-induced seismicity: Case of a heterogeneous fault. *Journal of Geophysical Research: Solid Earth*, *124*(8), 8426-8448.

Ampuero, J. P., & Rubin, A. M. (2008). Earthquake nucleation on rate and state faults aging and slip laws. *Journal of Geophysical Research-Solid Earth*, *113*.

Avouac, J. P., Vrain, M., Kim, T., Smith, J., Ader, T., Ross, Z., & Saarno, T. (2020). A convolution model for earthquake forecasting derived from seismicity recorded during the st1 geothermal project on otaniemi campus, finland. *In Proceedings World Geothermal Congress*, *1*.

Bachmann, C. E., Wiemer, S., Goertz-Allmann, B. P., & Woessner, J. (2012). Influence of pore-pressure on the event-size distribution of induced earthquakes. *Geophysical Research Letters*, *39*, 9.

Bachmann, C. E., Wiemer, S., Woessner, J., & Hainzl, S. (2011). Statistical analysis of the induced basel 2006 earthquake sequence: introducing a probability-based monitoring approach for enhanced geothermal systems. *Geophysical Journal International*, *186*(2), 793-807.

Baisch, S., & Harjes, H. P. (2003). A model for fluid-injection-induced seismicity at the ktb, germany. *Geophysical Journal International*, *152*(1), 160-170.

Baisch, S., Vörös, R., Rothert, E., Stang, H., Jung, R., & Schellschmidt, R. (2010). A numerical model for fluid injection induced seismicity at soultz-sous-forêts. *International Journal of Rock Mechanics and Mining Sciences*, *47*(3), 405-413.

Baisch, S., Weidler, R., Vörös, R., Wyborn, D., & de Graaf, L. (2006). Induced seismicity during the stimulation of a geothermal hfr reservoir in the cooper basin, australia. *Bulletin of the Seismological Society of America*, *96*(6), 2242-2256.

Beeler, N. M., & Lockner, D. A. (2003). Why earthquakes correlate weakly with the solid earth tides: Effects of periodic stress on the rate and probability of earthquake occurrence. *Journal of Geophysical Research: Solid Earth*, *108*.

Bertani, R. (2012). Geothermal power generation in the world 2005–2010 update report. geothermics. , *41*, 1-29.

Bommer, J. J., Oates, S., Cepeda, J. M., Lindholm, C., Bird, J., Torres, R., & Rivas, J. (2006). Control of hazard due to seismicity induced by a hot fractured rock geothermal project. *Engineering geology*, *83*(4), 287-306.

Bourne, S. J., Oates, S. J., & Van Elk, J. (2018). The exponential rise of induced seismicity with increasing stress levels in the groningen gas field and its implications for controlling seismic risk. *Geophysical Journal International*, *213*(3), 1693-1700.

Bourouis, S., & Bernard, P. (2007). Evidence for coupled seismic and aseismic fault slip during water injection in the geothermal site of soultz (france), and implications for seismogenic transients. *Geophysical Journal International*, *169*(2), 723-732.

Brace, W., Walsh, J. B., & Frangos, W. T. (1968). Permeability of granite under high pressure. *Journal of Geophysical research*, *73*(6), 2225-2236.

Calò, M., Dorbath, C., Cornet, F. H., & Cuenot, N. (2011). Large-scale aseismic motion identified through 4-dp-wave tomography. *Geophysical Journal International*, *186*(3), 1295-1314.

Candela, T., Osinga, S., Ampuero, J. P., Wassing, B., Pluymaekers, M., Fokker, P. A., & Muntendam-Bos, A. G. (2019). Depletion-induced seismicity at the groningen gas field: Coulomb rate-and-state models including differential compaction effect. *Journal of Geophysical Research: Solid Earth*, *124*(7), 7081-7104.

Cappa, F., Guglielmi, Y., Rutqvist, J., Tsang, C. F., & Thoraval, A. (2006). Hydromechanical modelling of pulse tests that measure fluid pressure and fracture normal displacement at the coaraze laboratory site, france. *International Journal of Rock Mechanics and Mining Sciences*, *43*(7), 1062-1082.

Cappa, F., Scuderi, M. M., Collettini, C., Guglielmi, Y., & Avouac, J. P. (2019). Stabilization of fault slip by fluid injection in the laboratory and in situ. *Science advances*, *5*, 3.

Cladouhos, T. T., Petty, S., Swyer, M. W., Uddenberg, M. E., Grasso, K., & Nordin, Y. (2016). Results from newberry volcano egs demonstration, 2010–2014. *Geothermics*, *63*, 44-61.

Cornet, F. H., & Jianmin, Y. (1995). Analysis of induced seismicity for stress field determination and pore pressure mapping. *In Mechanics Problems in Geodynamics Part I*, 677-700.

De Barros, L., Guglielmi, Y., Rivet, D., Cappa, F., & Duboeuf, L. (2018). Seismicity and fault aseismic deformation caused by fluid injection in decametric in-situ experiments. *Comptes Rendus Geoscience*, *350*(8), 464-475.

Dempsey, D., & Riffault, J. (2019). Response of induced seismicity to injection rate reduction: Models of delay, decay, quiescence, recovery, and oklahoma. *Water Resources Research*, *55*(1), 656-681.

Dempsey, D., & Suckale, J. (2017). Physics-based forecasting of induced seismicity at groningen gas field, the netherlands. *Geophysical Research Letters*, *44*(15), 7773-7782.

Dempsey, D., Suckale, J., & Huang, Y. H. (2016). Collective properties of injection-induced earthquake sequences: 2. *Spatiotemporal evolution and magnitude frequency distributions, Journal of Geophysical Research-Solid Earth*, *121*, 3638–3665.

Dieterich, J. (1994). A constitutive law for rate of earthquake production and its application to earthquake clustering. *Journal of Geophysical Research: Solid Earth*, *99*, 2601-2618.

Dieterich, J. H., & Linker, M. F. (1992). Fault stability under conditions of variable normal stress. *Geophysical Research Letters*, *19*(16), 1691-1694.

Dublanchet, P. (2018). The dynamics of earthquake precursors controlled by effective friction. *Geophysical Journal International*, *212*(2), 853-871.

Dublanchet, P., Bernard, P., & Favreau, P. (2013). Interactions and triggering in a 3-d rate-and-state asperity model. *Journal of Geophysical Research: Solid Earth*, *118*(5), 2225-2245.

Dublanchet, P., & De Barros, L. (2021). Dual seismic migration velocities in seismic swarms. *Geophysical Research Letters*, *48*, 1.

Elmar, E., & Shapiro, S. A. (2002). *Microseismic monitoring of borehole fluid injections: Data modeling and inversion for hydraulic properties of rocks.* OnePetro.

Elsworth, D., Spiers, C. J., & Niemeijer, A. R. (2016). Understanding induced seismicity. *Science*, *354*(6318), 1380-1381.

Evans, K. F., Moriya, H., Niitsuma, H., Jones, R. H., Phillips, W. S., Genter, A., & Baria, R. (2005). Microseismicity and permeability enhancement of hydrogeologic structures during massive fluid injections into granite at 3 km depth at the soultz hdr site. *Geophysical Journal International*, *160*(1), 388-412.

Gaucher, E., Schoenball, M., Heidbach, O., Zang, A., Fokker, P. A., van Wees, J. D., & Kohl, T. (2015). Induced seismicity in geothermal reservoirs: A review of forecasting approaches. *Renewable and Sustainable Energy Reviews*, *52*, 1473-1490.

Gens, A., Vaunat, J., Garitte, B., & Wileveau, Y. (2011). In situ behaviour of a stiff layered clay subject to thermal loading: observations and interpretation. *In Stiff Sedimentary Clays: Genesis and Engineering Behaviour: Géotechnique Symposium in Print*, *2007*, 123-144.

Goebel, T. H., & Brodsky, E. E. (2018). The spatial footprint of injection wells in a global compilation of induced earthquake sequences. *Science*, *361*(6405), 899-904.

Goodfellow, S. D., Nasseri, M. H. B., Maxwell, S. C., & Young, R. P. (2015). Hydraulic fracture energy budget: Insights from the laboratory. *Geophysical Research Letters*, *42*(9), 3179-3187.

Goodman, J., & Weare, J. (2010). Ensemble samplers with affine invariance. *Communications in applied mathematics and computational science*, *5*(1), 65-80.

Grigoli, F., Cesca, S., Priolo, E., Rinaldi, A. P., Clinton, J. F., Stabile, T. A., & Dahm, T. (2017). Current challenges in monitoring, discrimination, and management of induced seismicity related to underground industrial activities: A european perspective. *Reviews of Geophysics*, *55*(2), 310-340.

Grigoli, F., Cesca, S., Rinaldi, A. P., Manconi, A., Lopez-Comino, J. A., Clinton, J. F., & Wiemer, S. (2018). The november 2017 mw 5.5 pohang earthquake: A possible case of induced seismicity in south korea. *Science*, *360*(6392), 1003-1006.

Guglielmi, Y., Elsworth, D., Cappa, F., Henry, P., Gout, C., Dick, P., & Durand, J. (2015). In situ observations on the coupling between hydraulic diffusivity and displacements during fault reactivation in shales. *Journal of Geophysical Research: Solid Earth*, *120*(11), 7729-7748.

Gutenberg, B., & Richter, C. F. (1956). Earthquake magnitude, intensity, energy, and acceleration: (second paper). *Bulletin of the seismological society of Amer-*

ica, *46*(2), 105-145.

Healy, J. H., Rubey, W. W., Griggs, D. T., & Raleigh, C. B. (1968). The denver earthquakes. *Science*, *161*(3848), 1301-1310.

Heimisson, E. R., & Segall, P. (2018). Constitutive law for earthquake production based on rate-and-state friction: Dieterich 1994 revisited. *Journal of Geophysical Research: Solid Earth*, *123*(5), 4141-4156.

Heimisson, E. R., Smith, J. D., Avouac, J. P., & Bourne, S. J. (2022). Coulomb threshold rate-and-state model for fault reactivation: application to induced seismicity at groningen. *Geophysical Journal International*, *228*(3), 2061-2072.

Hillers, G., Vuorinen, T., A., T., Uski, M. R., Kortström, J. T., Mäntyniemi, P. B., ... Saarno, T. (2020). The 2018 geothermal reservoir stimulation in espoo/helsinki, southern finland: Seismic network anatomy and data features. *Seismological Research Letters*, *91*(2), 770-786.

Horne, R. N. (1995). Modern well test analysis. *Petroway Inc*, *926*.

Häring, M. O., Schanz, U., Ladner, F., & Dyer, B. C. (2008). Characterisation of the basel 1 enhanced geothermal system. *Geothermics*, *37*(5), 469-495.

Im, K., Elsworth, D., Guglielmi, Y., & Mattioli, G. S. (2017). Geodetic imaging of thermal deformation in geothermal reservoirs-production, depletion and fault reactivation. *Journal of Volcanology and Geothermal Research*, *338*, 79-91.

Jr, M., & J., F. (1951). The kolmogorov-smirnov test for goodness of fit. *Journal of the American statistical Association*, *46*(253), 68-78.

Kwiatek, G., Saarno, T., Ader, T., Bluemle, F., Bohnhoff, M., Chendorain, M., & Wollin, C. (2019). Controlling fluid-induced seismicity during a 6.1-km-deep geothermal stimulation in finland. *Science Advances*, *5*, 5.

Langenbruch, C., & Shapiro, S. A. (2010). Decay rate of fluid-induced seismicity after termination of reservoir stimulations. *Geophysics*, *75*, 6.

Larochelle, S., Lapusta, N., Ampuero, J. P., & Cappa, F. (2021). Constraining fault friction and stability with fluid-injection field experiments. *Geophysical Research Letters*, *2020*.

Lavrov, A. (2003). The kaiser effect in rocks: principles and stress estimation techniques. *International Journal of Rock Mechanics and Mining Sciences*, *40*(2), 151-171.

Lei, X., Yu, G., Ma, S., Wen, X., & Wang, Q. (2008). Earthquakes induced by water injection at $\sim$ 3 km depth within the rongchang gas field, chongqing, china. *Journal of Geophysical Research: Solid Earth*, *113*.

Leonhardt, M., Kwiatek, G., Martínez-Garzón, P., Bohnhoff, M., Saarno, T., Heikkinen, P., & Dresen, G. (2021). Seismicity during and after stimulation of a 6.1 km deep enhanced geothermal system in helsinki, finland. *Solid Earth*, *12*(3), 581-594.

Majer, E. L., Baria, R., Stark, M., Oates, S., Bommer, J., Smith, B., & Asanuma, H. (2007). Induced seismicity associated with enhanced geothermal systems. *Geothermics*, *36*(3), 185-222.

Marone, C. (1998). The effect of loading rate on static friction and the rate of fault healing during the earthquake cycle. *Nature*, *391*(6662), 69-72.

Marsan, D., & Lengline, O. (2008). Extending earthquakes' reach through cascading. *Science*, *319*(5866), 1076-1079.

McClure, M. W., & Horne, R. N. (2011). Investigation of injection-induced seismicity using a coupled fluid flow and rate/state friction model. *Geophysics*, *76*, 6.

Mena, B., Wiemer, S., & Bachmann, C. (2013). Building robust models to forecast the induced seismicity related to geothermal reservoir enhancement. *Bulletin of the Seismological Society of America*, *103*(1), 383-393.

Miller, S. A. (2013). The role of fluids in tectonic and earthquake processes. In *Advances in geophysics* (p. 1-46). Elsevier: 54.

Miller, S. A. (2020). Aftershocks are fluid-driven and decay rates controlled by permeability dynamics. *Nature Communications*, *11*(1), 1-11.

Mohamed, I. M., Block, G. I., Abou-Sayed, O. A., Elkatatny, S. M., & Abou-Sayed, A. S. (2016). Flow rate-dependent skin in water disposal injection well. *Journal of Energy Resources Technology*, *138*, 5.

Norbeck, J. H., & Rubinstein, J. L. (2018). Hydromechanical earthquake nucleation model forecasts onset, peak, and falling rates of induced seismicity in oklahoma and kansas. *Geophysical Research Letters*, *45*(7), 2963-2975.

Nur, A., & Booker, J. R. (1972). Aftershocks caused by pore fluid flow? *Science*, *175*(4024), 885-887.

Ogata, Y. (1988). Statistical models for earthquake occurrences and residual analysis for point processes. *Journal of the American Statistical association*, *83*(401), 9-27.

Olsen, K. B., Madariaga, R., & Archuleta, R. J. (1997). Three-dimensional dynamic simulation of the 1992 landers earthquake. *Science*, *278*, 834–838.

Perfettini, H., & Avouac, J. P. (2004). Postseismic relaxation driven by brittle creep: A possible mechanism to reconcile geodetic measurements and the decay rate of aftershocks, application to the chi-chi earthquake, taiwan. *Journal of Geophysical Research: Solid Earth*, *109*.

Raleigh, C. B., Healy, J. H., & Bredehoeft, J. D. (1976). An experiment in earthquake control at rangely, colorado. *Science*, *191*(4233), 1230-1237.

Renard, P., Glenz, D., & Mejias, M. (2009). Understanding diagnostic plots for well-test interpretation. *Hydrogeology Journal*, *17*(3), 589-600.

Richter, G., Hainzl, S., Dahm, T., & Zöller, G. (2020). Stress-based, statistical modeling of the induced seismicity at the groningen gas field, the netherlands. *Environmental Earth Sciences*, *79*(11), 1-15.

Ross, Z. E., Meier, M. A., & Hauksson, E. (2018). P wave arrival picking and first-motion polarity determination with deep learning. *Journal of Geophysical Research: Solid Earth*, *123*(6), 5120-5129.

Ross, Z. E., Meier, M. A., Hauksson, E., & Heaton, T. H. (2018). Generalized seismic phase detection with deep learning. *Bulletin of the Seismological Society of America*, *108*(5), 2894-2901.

Rudnicki, J. W. (1986). Fluid mass sources and point forces in linear elastic diffusive solids. *Mechanics of Materials*, *5*(4), 383-393.

Ruina, A. (1983). Slip instability and state variable friction laws. *Journal of Geophysical Research: Solid Earth*, *88*, 10359-10370.

Rutqvist, J., & Oldenburg, C. M. (2008, June). Analysis of injection-induced microearthquakes in a geothermal steam reservoir, the geysers geothermal field, california. *42nd U.S. Rock Mechanics Symposium (USRMS), San Francisco, California*.

Sander, M. (2011). Geothermal energy in recent international energy strategies; geothermie in aktuellen internationalen energiestrategien. *Geothermische Energie*, *20*.

Schultz, R., Skoumal, R. J., Brudzinski, M. R., Eaton, D., Baptie, B., & Ellsworth, W. (2020). Hydraulic fracturing-induced seismicity. *Reviews of Geophysics*, *58*, 3.

Scotti, O., & Cornet, F. H. (1994, August). In situ evidence for fluid-induced aseismic slip events along fault zones. *International journal of rock mechanics and mining sciences geomechanics abstracts*, *31*(4), 347-358.

Segall, P. (1989). Earthquakes triggered by fluid extraction. *Geology*, *17*(10), 942-946.

Segall, P., Desmarais, E. K., Shelly, D., Miklius, A., & Cervelli, P. (2006). Earthquakes triggered by silent slip events on kīlauea volcano, hawaii. *Nature*, *442*(7098), 71-74.

Segall, P., Grasso, J. R., & Mossop, A. (1994). Poroelastic stressing and induced seismicity near the lacq gas field, southwestern france. *Journal of Geophysical Research: Solid Earth*, *99*, 15423-15438.

Segall, P., & Lu, S. (2015). Injection-induced seismicity: Poroelastic and earthquake nucleation effects. *Journal of Geophysical Research: Solid Earth*, *120*(7), 5082-5103.

Shapiro, S. A., Audigane, P., & Royer, J. J. (1999). Large-scale in situ permeability tensor of rocks from induced microseismicity. *Geophysical Journal International*, *137*(1), 207-213.

Shapiro, S. A., Dinske, C., & Rothert, E. (2006). Hydraulic-fracturing controlled dynamics of microseismic clouds. *Geophysical Research Letters*, *33*, 14.

Shapiro, S. A., Huenges, E., & Borm, G. (1997). Estimating the crust permeability from fluid-injection-induced seismic emission at the ktb site. *Geophysical Journal International*, *131*(2), F15-F18.

Shapiro, S. A., Rothert, E., Rath, V., & Rindschwentner, J. (2002). Characterization of fluid transport properties of reservoirs using induced microseismicity. *Geophysics*, *67*(1), 212-220.

Skempton, A. (1984). Effective stress in soils, concrete and rocks. *Selected papers on soil mechanics*, *1032*, 4-16.

Smith, J. D., White, R. S., Avouac, J. P., & Bourne, S. (2020). Probabilistic earthquake locations of induced seismicity in the groningen region, the netherlands. *Geophysical Journal International*, *222*(1), 507-516.

Stefanou, I. (2019). Controlling anthropogenic and natural seismicity: Insights from active stabilization of the spring-slider model. *Journal of Geophysical Research: Solid Earth*, *124*(8), 8786-8802.

Tester, J. W., Anderson, B. J., Batchelor, A. S., Blackwell, D. D., DiPippo, R., Drake, E. M., & Toksoz, M. N. (2006). The future of geothermal energy. *Massachusetts Institute of Technology*, *358*.

Toda, S., Stein, R. S., & Sagiya, T. (2002). Evidence from the ad 2000 izu islands earthquake swarm that stressing rate governs seismicity. *Nature*, *419*(6902), 58-61.

Utsu, T. (2002). Statistical features of seismicity. *International geophysics series*, *81*, 719-732.

Vilarrasa, V., & Carrera, J. (2015). Geologic carbon storage is unlikely to trigger large earthquakes and reactivate faults through which co2 could leak. *Proceedings of the National Academy of Sciences*, *112*(19), 5938-5943.

Waldhauser, F., & Ellsworth, W. L. (2000). A double-difference earthquake location algorithm: Method and application to the northern hayward fault, california. *Bulletin of the seismological society of America*, *90*(6), 1353-1368.

Wei, S., Avouac, J. P., Hudnut, K. W., Donnellan, A., Parker, J. W., Graves, R. W., & Eneva, M. (2015). The 2012 brawley swarm triggered by injection-induced aseismic slip. *Earth and Planetary Science Letters*, *422*, 115-125.

Wenzel, F. (2017). Fluid-induced seismicity: comparison of rate-and state-and critical pressure theory. *Geothermal Energy*, *5*(1), 1-16.

White, J. A., & Foxall, W. (2016). Assessing induced seismicity risk at co2 storage projects: Recent progress and remaining challenges. *International Journal of Greenhouse Gas Control*, *49*, 413-424.

Wiemer, S., Kraft, T., & Landtwing, D. (2015). *Energy from the earth. deep geothermal as a resource for the future?* (Vol. 62; S. Hirschberg, S. Wiemer, & P. Burgherr, Eds.). vdf Hochschulverlag AG an der ETH Zürich.

Zaliapin, I., & Ben-Zion, Y. (2013). Earthquake clusters in southern california i: Identification and stability. *Journal of Geophysical Research: Solid Earth*, *118*(6), 2847-2864.

Zang, A., Oye, V., Jousset, P., Deichmann, N., Gritto, R., McGarr, A., & Bruhn, D. (2014). Analysis of induced seismicity in geothermal reservoirs–an overview. *Geothermics*, *52*, 6-21.

Zbinden, D., Rinaldi, A. P., Diehl, T., & Wiemer, S. (2020). Hydromechanical modeling of fault reactivation in the st. *Gallen deep geothermal project (Switzer-*

land): poroelasticity or hydraulic connection?. Geophysical Research Letters, *47*, 3.

Zhai, G., & Shirazei, M. (2018). Fluid injection and time-dependent seismic hazard in the barnett shale, texas. *Geophysical Research Letters*, *45*(10), 4743-4753.

Zimmerman, R. W. (2018). *Imperial college lectures in petroleum engineering, the-volume 5: Fluid flow in porous media*. World Scientific.

Zoback, M. D., & Gorelick, S. M. (2012). Earthquake triggering and large-scale geologic storage of carbon dioxide. *Proceedings of the National Academy of Sciences*, *109*(26), 10164-10168.

Zoller, G., Holschneider, M., & Ben-Zion, Y. (2005). The role of heterogeneities as a tuning parameter of earthquake dynamics. *Pure and Applied Geophysics*, *162*, 1027–1049.